New computational tools and experiments reveal how geometry affects tissue growth in 3D printed scaffolds

Daniel J. VandenHeuvel[a], Brenna L. Devlin[b], Pascal R. Buenzli[a], Maria A. Woodruff[b], Matthew J. Simpson[a,*]

[a]*School of Mathematical Sciences, Queensland University of Technology (QUT), Brisbane, Australia.*
[b]*School of Mechanical Medical and Process Engineering, QUT, Brisbane, Australia.*

Abstract

Understanding how tissue growth in porous scaffolds is influenced by geometry is a fundamental challenge in the field of tissue engineering. We investigate the influence of pore geometry on tissue growth using osteoblastic cells in 3D printed melt electrowritten scaffolds with square-shaped pores and non-square pores with wave-shaped boundaries. Using a reaction-diffusion model together with a likelihood-based uncertainty quantification framework, we quantify how the cellular mechanisms of cell migration and cell proliferation drive tissue growth for each pore geometry. Our results show that the rates of cell migration and cell proliferation appear to be largely independent of the pore geometries considered, suggesting that observed curvature effects on local rates of tissue growth are due to space availability rather than directly affecting cell behaviour. This result allows for simple squared-shaped pores to be used for estimating parameters and making predictions about tissue growth in more realistic pores with more realistic, complicated shapes. Our findings have important implications for the development of predictive tools for tissue engineering and experimental design, highlighting new avenues for future research.

Keywords: Tissue engineering; Mathematical modelling; Curvature; Tissue growth; Pore geometry

1. Introduction

Tissue engineering aims to regenerate damaged or diseased tissues [1]. A key challenge in tissue engineering is to understand how various clinically-motivated experimental conditions influence tissue growth [2]. Recent advancements in three-dimensional (3D) printing allow us to investigate tissue growth in 3D-printed scaffolds of various shapes and sizes, enabling realistic migration and proliferation behaviours to be studied in well-controlled experimental conditions [3, 4]. While the effect of pore geometry and tissue curvature on tissue growth is well-known [5–7], understanding how these effects relate to cellular-level mechanisms remains poorly understood. Understanding these cellular mechanisms would enable the prediction and analysis of tissue growth in complex geometries from the calibration of mathematical models in simpler geometries, providing a valuable computational tool for screening experimental designs [8] of scaffold geometries and providing plausible results on these new geometries. This kind

---

*Corresponding author. Email: matthew.simpson@qut.edu.au

of computational tool could enable more personalised approaches to tissue engineering, in which a specific scaffold size and shape could be tailored to an individual patient, making use of these predictions to screen for possible patient outcomes.

3D printing technology for biofabrication has evolved rapidly [9, 10]. Melt electrowriting, a technique for high quality 3D printing, allows for micro- and nano-scale fibres to created, enabling great control over the fibres and the pore geometry, making it possible to produce realistic scaffold geometries with a regular array of pores for growing tissue [11–14]. These scaffolds are designed so that cells and tissues experience a similar mechanical support as they would, for example, in skin and bone tissues, enabling realistic cell migration and cell proliferation behaviours to be observed and measured [3]. Previous work has focused primarily on squared-shaped pores [15, 16], although more complicated scaffolds can also be produced [10, 17]. One important factor in understanding tissue growth is curvature [18, 19]. In the context of bone tissue, Bidan et al. [20] suggest that cell tension can influence tissue curvature that, in turn, can stimulate tissue growth. Callens et al. [21] discuss how cells respond to their surrounding geometry, even across large spatial scales, and how this affects bone tissue growth. Mathematical modelling studies performed by Alias and Buenzli [22–24] and Hegarty-Cremer et al. [25] also investigate the role of geometry and curvature on tissue growth and cell crowding in bone tissue growth experiments.
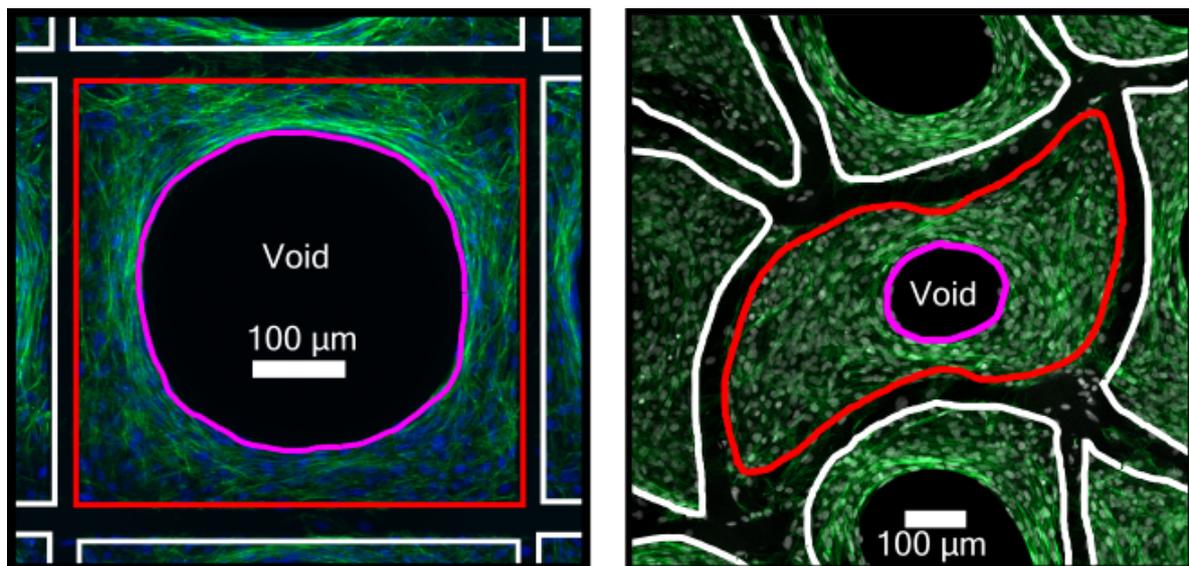

Figure 1: Scaffold pore boundary (red boundary), void (black interior), void boundary (magenta boundary), tissue (blue/green region), and fibres (exterior black boundary). The white outlines show the scaffold boundaries. The blue channel in the microscope images shows the cell nuclei (DAPI), and the green channel shows the tissue and cytoskeleton (phalloidin). The DAPI on the right image is shown in grey.

Tissue growth experiments in porous scaffolds are of great importance in tissue engineering [16, 26]. In these experiments, cells are seeded onto the perimeter of a scaffold, leading to cell migration and cell proliferation that produces an inward-growing tissue. The shape of the region that is devoid of cell and tissue material, referred to as the *void* in Figure 1, matches the shape of the scaffold boundary for early times, rounding off over time, eventually

forming a circular front until the void closes, which we call *pore bridging*. The feature of interest in these experiments is the time that the tissue bridges, called the *bridging time* [16, 26]. A circular front arises with time in many pore scaffold geometries such as square, triangular, and hexagonally shaped pores [15, 16, 27, 28], though the precise mechanisms driving the cells into these circular fronts in general geometries remains unclear. The most common way to report a set of pore bridging experiments is to record snapshot images of the tissue growth process [15, 16, 26]. This approach allows us to estimate the bridging time within an interval instead of identifying the precise time of bridging [16, 26], thereby introducing some uncertainty into the experimental estimate of the bridging time. To interpret such measurements meaningfully, we are interested in developing mathematical modelling tools that mechanistically capture cell migration and cell proliferation within a framework that explicitly incorporates uncertainty in the experimental measurements, uncertainty in the parameter estimates in the mathematical model, and that is capable of making predictions of new experiments that incorporate these uncertainties. This will allow us, for example, to study how variability in bridging times can be explicitly integrated into the mathematical model, as well as interpreting the predictions of the mathematical model.

In this paper, we study mechanistic cell behaviour in pore bridging experiments performed within pores on 3D-printed scaffolds made from polycaprolactone [4, 10, 26]. We consider tissue growth in two different shaped pores, a square-shaped pore (Figure 1(a)) and a wave-shaped pore (Figure 1(b)), with the aim to understand whether the details of cell migration and cell proliferation are affected by differences in the pore geometry. In particular, we are interested in determining whether the cellular mechanisms driving tissue growth in the more realistic wave-shaped pore are indistinguishable from the cellular mechanisms driving tissue growth in the simpler square geometry. Moreover, we are interested in obtaining estimates of bridging time with uncertainty, for both pore geometries, through probability distributions that allow a user to predict probabilities of bridging time occurring within a specified time window for any pore geometry. All experiments reported in this paper involve tissue growth using murine calvarial osteoblastic cells (MC3T3-E1) [29]. Our group has previously used these experiments on the square pores with different sizes [15, 16, 26], investigating the relationship between the cell migration rate measured in terms of the cell diffusivity D, cell proliferation rate λ, and scaffold size. This previous work showed that the product $D\lambda$, which controls the long-time rate of tissue production, appeared to be unaffected by the pore size, but did not consider the role of pore shape. These previous experiments displayed variability in the time to bridge, even in well controlled experiments with the same pore size. This variability motivates the need for developing mathematical modelling tools that incorporate variability and uncertainty quantification into predictions. Hence, our analysis uses a combination of numerical simulations from a mathematical model and with statistical analysis that takes numerical simulations and quantifies results together with uncertainty. These considerations will be used to answer the following broad questions:

1. Are the cellular mechanisms driving tissue growth independent of pore shape?

2. Can we use results on one pore shape to make predictions, with uncertainty, on another geometry?

3. What data, and how much data, is sufficient for accurately comparing results for different shaped pores?

We address these questions using a model-based approach, using the Porous-Fisher partial differential equation (PDE) as a model for tissue growth driven by combined cell migration and cell proliferation [30]. Solving this mathematical model requires parameter estimates for the cell diffusivity, D, the cell proliferation rate, λ, and the initial cell density on the scaffold boundary, u_0. Estimates for D and λ cannot be obtained directly from experimental images, hence methods that use information about the images are needed. For each pore shape, we calibrate this mathematical model with an experimental dataset containing information about the position of the tissue front over time. We apply a likelihood-based analysis to this dataset [31] with the aim to estimate the combined effect of proliferation and migration rates, by estimating the product $D\lambda$. Profile likelihoods are used to quantify the uncertainty in $D\lambda$, providing confidence intervals for $D\lambda$ [32], and allowing us to determine what parameters or parameter combinations can be estimated [33, 34], providing insights into the second and third research questions listed above. The confidence intervals obtained on each geometry can be used to compare the tissue growth mechanisms for each pore geometry to answer the first research question. This analysis also enables us to make predictions with uncertainty about the pore bridging time. By using this likelihood-based approach to make predictions, we can take results from the square-shaped pores and estimate, with uncertainty, the pore bridging times on the wave-shaped pores. Similarly, we can use the wave-shaped pores to make predictions on the square-shaped pores. Comparing both situations allows us to answer the second research question. The simplest interpretation of our results is that the cell migration and cell proliferation rates are independent of the pore scaffold geometry.

2. Materials and Methods

In this section, we describe the methods used for the experiments and the data that we collect from these experiments. Following this description, we introduce the mathematical models we use and how we apply likelihood analysis for performing statistical inference from these experiments.

2.1. Tissue growth experiments

All reagents are sourced from Thermo Fisher unless otherwise stated. Using a melt electrowriting printer described previously [26], polycaprolactone (45 kDa, Sigma Aldrich) fibres of diameter 50 μm are fabricated into a three-layer scaffold which was then biopsy punched to form a 6 mm disc. The resultant scaffold has a thickness of approximately 150 μm. The code used to produce the outline of each pore is adjusted to produce square-shaped and wave-shaped pores of comparable size, both being derived from a unit of cell of 500 μm. Prior to cell seeding, scaffolds are sterilised under UV light overnight. The cells used are murine calvarial osteoblastic cells (MC3T3-E1) [29] that are cultured in α-MEM, 10 % fetal bovine serum, and 1 % penicillin-streptomycin, and are approximately 20–30 μm in diameter [26]. Cells were expanded in a T75 culture flask and at 80 % confluency were detached with TrypLE. Cells were seeded at a density of 10,000 cells per scaffold in 48-well plates. After allowing 4 h for the cells to attach to each scaffold after seeding, an additional 500 μL was added. Cell-seeded scaffolds were cultured in a humidified environment at 37 °C in 5 % CO2 for 28 days. The media is changed every 2–3 days from day 5 to day 14, every 1–2

days from day 15 to 28. The viability of the cells are assessed at day 10, 14, and 28 using calcein-AM and ethidium homodimer-1 to stain live and dead cells, respectively. At specific timepoints, cell-seeded scaffolds were fixed with 4 % paraformaldehyde and stained with 4',6-diamidino-2-phenylindole (DAPI) and Alexa Fluor™ 488 Phalloidin, which stain cell nuclei and actin filaments, respectively. High resolution images of the centre of each scaffold are obtained using fluorescent microscopy (Zeiss, AxioObserver 7). For each pore shape and timepoint, fixation, staining, and microscopy are repeated across two or three identically prepared replicates. Each experimental replicate provides information of several pores, giving information about tissue growth data from day 5 to day 28. This procedure gives 41 data points for the square pore, and 3 data points for the wave pore; while this number of data points is relatively small, it is sufficient for our analysis as we use a likelihood-based uncertainty quantification framework that naturally incorporates variability associated with finite sample sizes, as introduced in Section 2.4. More information on the procedure for capturing these images is provided in [26]. These experiments lead to a tissue composed of a monolayer of cells within the pore. The growth of monolayers is achieved through the design of the pore geometry as the width of the pores is large compared to the pore depth. The vertical pore depth is approximately equal to the average cell diameter, 20–30 μm [26], which means that we do not observe cells growing on top of each other in the vertical direction.

2.2. Data and image processing

The experiments provide us with several images at four time points (days 7, 14, 25, and 28), and each image contains information about several pores. To summarise the tissue growth processes, for each pore we calculate two quantities:

$$y_c^{i,j} = \frac{\text{area of void}}{\text{area of pore}}, \quad y_p^{i,j} = \frac{\text{perimeter of void}}{\text{perimeter of pore}}, \tag{1}$$

where $y_c^{i,j}$ and $y_p^{i,j}$ denote the *void coverage* and *normalised void perimeter*, respectively, for the jth pore at the ith time, t_i. We do not collect data from any pores that have bridged, or pores that have bridged in a way so that the void splits into multiple disconnected regions. All images at $t = 25$ day and $t = 28$ day show that all pores have bridged before 25 days, so we focus on measuring (1) at $t_1 = 7$ day and $t_2 = 14$ day. A precise description of how we compute the quantities in (1) from the images is given in Section S1 of the Supplementary Material.

To complete the processing, we select the computational representations for the square and wave geometries for use in the mathematical model described Section 2.3 (Figure 2) for comparison with each data point. In the square case, we construct this independent of the images, and simply define a boundary for a square with its lower-left corner at the origin and side length $L = 475$ μm. For the wave geometry, we take a single image from the experiments and choose its boundary as a representative boundary for each experiment, which is reasonable as all scaffolds are uniformly printed.

2.3. Mathematical model

We use the Porous-Fisher PDE to model tissue growth, as this model explicitly describes how cell migration and cell proliferation leads to tissue growth with sharp fronts that we observe in the experiments (Figures 3 and 4) [15, 30]. Since the pore bridging process starts after 5 days, the PDE is solved for $t > 5$ day. Letting $\tilde{u}(x, y, t)$ [cells/μm^2] denote the density of cells at a point (x, y) and time t [day], and $\tilde{K}$ denoting the maximum carrying capacity density [cells/μm^2], we define a normalised density $u(x, y, t) \in [0, 1]$ by $u(x, y, t) = \tilde{u}(x, y, t)/\tilde{K}$. Thus, the model for $u(x, y, t)$ is given by

$$\frac{\partial u(x,y,t)}{\partial t} = D \underbrace{\left\{ \frac{\partial}{\partial x} \left[u(x,y,t) \frac{\partial u(x,y,t)}{\partial x} \right] + \frac{\partial}{\partial y} \left[u(x,y,t) \frac{\partial u(x,y,t)}{\partial y} \right] \right\}}_{\text{contact stimulated cell migration}} + \underbrace{\lambda u(x,y,t) \left[1 - u(x,y,t) \right]}_{\text{contact inhibited cell proliferation}}, \quad (x,y) \in \Omega, \quad (2)$$

$$\frac{\mathrm{d}u(x,y,t)}{\mathrm{d}t} = \underbrace{\lambda u(x,y,t) \left[1 - u(x,y,t) \right]}_{\text{contact inhibited cell proliferation}}, \quad (x,y) \in \partial\Omega, \quad (3)$$

$$u(x,y,5) = \begin{cases} u_0 & (x,y) \in \partial\Omega, \\ 0 & (x,y) \in \Omega. \end{cases} \quad (4)$$

where (2) is applied on the interior scaffold pore space Ω, the space inside the red curves of Figure 2; (3) is applied on the boundary $\partial\Omega$, the red curve in Figure 2. We note that while our scaffolds are three-dimensional, their thickness is small compared to their width, and so this two-dimensional depth-averaged model (2)–(4) is reasonable [35]. This model is characterised by three parameters (D, λ, u_0), where D [μm^2/day] is the cell diffusivity that controls the rate of cell migration, λ [day^{-1}] is the cell proliferation rate, and u_0 is the normalised density of cells on the scaffold boundary $\partial\Omega$ at $t = 5$ day. We solve Equations (2)–(4) numerically using the finite volume method with an unstructured triangular mesh (Figure 2), as described in Section S2 of the Supplementary Material.
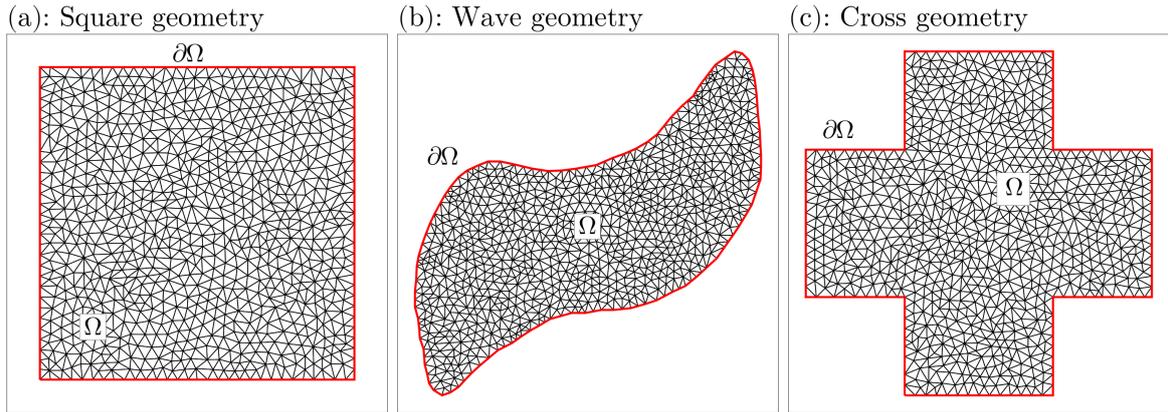

Figure 2: Schematics for triangular meshes used for numerical solutions of Equations (2)–(4) on the (a) square-shaped pore, (b) the wave-like pore, and (c) the cross-shaped pore considered in Section 3.3. Denser meshes are used for the actual solutions. The triangles represent the mesh we use for studying these geometries computationally, as discussed in Section 2.3. The red curves represent the boundary $\partial\Omega$, and the region bounded by these curves is the interior domain Ω.

Solutions of Equations (2)–(4) are used to compute model predictions corresponding to the data $y_c^{i,j}$ and $y_p^{i,j}$ from (1). Using the numerical solution for $u(x, y, t)$, we identify the contour $u(x, y, t) = 1/2$ to indicate the location of the tissue front [15, 16]. We define predictions of the $y_c^{i,j}$ and $y_p^{i,j}$ by

$$\mu_c(t) = \frac{1}{A(\Omega)} \sum_{k=1}^n A_k(t), \quad \mu_p(t) = \frac{1}{\ell(\partial\Omega)} \sum_{k=1}^n \ell_k(t), \tag{5}$$

respectively, where n is the number of triangular elements in the mesh, $A_k(t)$ is the area of the portion of the kth element at the time t that is inside the contour $u(x, y, t) = 1/2$, $\ell_k(t)$ is the length of the line through the kth element at the time t that is on the contour $u(x, y, t) = 1/2$ or zero if the contour does not go through the element, and $A(\Omega)$ and $\ell(\partial\Omega)$ are the area and perimeter of the domain Ω, respectively. More details on how we compute the coverage μ_c and normalised perimeter μ_p are given in Section S3 of the Supplementary Material.

We remark that our definition of the PDE (2)–(4) involves working with a nondimensional dependent variable u and nondimensional parameter u_0, while retaining the dimensional parameters D and λ and dimensional variables x, y, and t, so that spatial and temporal features can be compared with experimental images, similar to [36]. Our interpretation of the dependent variable, $u(x, y, t)$, is different, though. While it is possible to work with the dimensional density $\tilde{u}(x, y, t)$ [15, 37], this would require manually counting cells to estimate cell densities in space and time [36, 38, 39]. Thus, to be consistent with the fact that we only treat the leading edge in the experimental images for computing $y_c^{i,j}$ and $y_p^{i,j}$, it makes sense to consider the dimensionless ratio $u(x, y, t) = \tilde{u}(x, y, t)/\tilde{K}$ rather than $\tilde{u}(x, y, t)$ itself.

2.4. Parameter estimation

We use a likelihood-based approach to estimate model parameters [33, 40]. This approach takes predictions $\mu_c(t)$ and $\mu_p(t)$ from solutions of Equations (2)–(4) and compares them with the noisy experimental observations, $y_c^{i,j}$ and $y_p^{i,j}$. We assume that these noisy experimental observations are all independent realisations of random variables Y_c^i and Y_p^i, respectively, that are defined by [15]

$$Y_c^i \sim \mathcal{N}\left(\mu_c(t_i; \boldsymbol{\theta}), \sigma_c^2\right), \quad \text{and} \quad Y_p^i \sim \mathcal{N}\left(\mu_p(t_i; \boldsymbol{\theta}), \sigma_p^2\right), \tag{6}$$

where $\mathcal{N}(\mu, \sigma^2)$ denotes the normal distribution with mean μ and variance σ^2. These random variables in (6) each have a mean that depends on $\boldsymbol{\theta} = (D, \lambda, u_0)$, and the variances σ_c^2 and σ_p^2 need to be estimated. The values of σ_c and σ_p are treated as constants that are pre-estimated using the sample standard deviation of the experimental data aggregated for each t_i and each j, as described in Section S3 of the Supplementary Material.

Given sufficient experimental data we could, in theory, estimate all model parameters $\boldsymbol{\theta}$ and σ_c^2 and σ_p^2 directly, however, as we will show, our data is insufficient for this purpose. We find that our numerical simulations of Equations (2)–(4) on the time scale of our experiments are relatively independent of u_0, and so we show results for a range of pre-specified values of u_0 rather than focusing on any single value, demonstrating this independence. While it would be ideal to estimate both D and λ, we find that it is difficult to treat them separately, as we show in Section S4 of the Supplementary Material [16, 37]. For our purposes, though, we are mainly interested in the combined effect $D\lambda$,

as this is the variable that affects the velocity of the tissue and thus the bridging time [16]. Thus, rather than using $\boldsymbol{\theta} = (D, \lambda, u_0)$, we instead re-parametrise the vector of model parameters as $\boldsymbol{\theta} = (D\lambda, \lambda)$, omitting u_0 and following [41]. With this definition, $\mu_c(t_i; \boldsymbol{\theta})$ and $\mu_p(t_i; \boldsymbol{\theta})$ still refer to predictions from the solution of the PDE with parameters D and λ, and the choice of the fixed value of u_0 is left implicit.

2.4.1. Log-likelihood function

The log-likelihood function $\ell(\boldsymbol{\theta} \mid \mathbf{y})$ is a function of the model parameters that describes the likelihood that the model has parameter values $\boldsymbol{\theta}$ given that the data observed is $\mathbf{y}$ [31, 42]. In this work we have

$$\ell(\boldsymbol{\theta} \mid \mathbf{y}) = \sum_{i=1}^{2} \sum_{j=1}^{J(i)} \left[\log \phi \left(y_c^{i,j}; \mu_c(t_i; \boldsymbol{\theta}), \sigma_c^2 \right) + \log \phi \left(y_p^{i,j}; \mu_p(t_i; \boldsymbol{\theta}), \sigma_p^2 \right) \right], \tag{7}$$

where $\mathbf{y}$ is the vector of observations, $\phi(x; \mu, \sigma^2) = (2\pi\sigma^2)^{-1/2} \exp\left[-(x - \mu)^2/(2\sigma^2)\right]$ is the normal probability density function, and $J(i)$ is the number of pores included at the time t_i. For the wave pore, the log-likelihood (7) only includes the sum at $i = 2$ as there is only data at $t_2 = 14$ day in this case. For notational convenience we write $\ell(\boldsymbol{\theta} \mid \mathbf{y})$ as $\ell(\boldsymbol{\theta})$. The log-likelihood depends on the parameters $\boldsymbol{\theta} = (D\lambda, \lambda)$ and the fixed values for u_0, σ_c, and σ_p, with $\{D, \lambda, u_0\}$ governing the solution to the PDE and σ_p and σ_c governing the measurement model.

2.4.2. Maximum likelihood estimation

We obtain a best-fit estimate for the parameters $\boldsymbol{\theta}$ by maximising $\ell(\boldsymbol{\theta})$. This procedure is called maximum likelihood estimation [31], and it results in a maximum likelihood estimate (MLE) for $\boldsymbol{\theta}$, denoted $\hat{\boldsymbol{\theta}}$. For this maximisation, we constrain the values of D and λ so that $0 \, \mu\text{m}^2/\text{day}^2 < D\lambda \leqslant 10\,000 \, \mu\text{m}^2/\text{day}^2$. For λ we use $0 \, \text{day}^{-1} < \lambda \leqslant 5 \, \text{day}^{-1}$ in the square and $0 \, \text{day}^{-1} < \lambda \leqslant 10 \, \text{day}^{-1}$ in the wave. These bounds do not affect the results significantly. More detail on how we perform this maximum likelihood estimation is given in Section S5 of the Supplementary Material.

2.4.3. Uncertainty quantification

One limitation of maximum likelihood estimation is that we obtain a single point estimate for the MLE $\hat{\boldsymbol{\theta}}$, and the asymptotic uncertainty in this point estimate depends upon the curvature of the log-likelihood function [43]. To quantify the uncertainty in this estimate, we combine two approaches. For the first approach, we evaluate the log-likelihood function $\ell(\boldsymbol{\theta})$ over a large grid of $D\lambda$ and λ values. We then use this grid to find all points where $\ell(\boldsymbol{\theta}) - \ell^* \geqslant -\chi_{2,1-\alpha}^2/2$, where $\chi_{d,q}^2$ is the qth quantile of the χ^2 distribution with d degrees of freedom and $\ell^* = \ell(\hat{\boldsymbol{\theta}})$ is the maximum likelihood, as the resulting set of values defines a $100(1 - \alpha)\%$ credible region (CR) for $\boldsymbol{\theta}$ [31, 44]. We use $\alpha = 0.05$ in this work, giving $-\chi_{2,0.95}^2/2 \approx -3$.

The approach above gives us a two-dimensional region representing the uncertainty in $\boldsymbol{\theta}$. It will also be useful to reduce these regions to confidence intervals for each parameter, and most importantly for the parameter combination $D\lambda$, which allows us to make predictions about the variability in tissue growth later in Section 2.4.5. We take a profile likelihood approach to consider each parameter individually, specifying a range of values for an interest parameter

and using numerical optimisation, reducing the log-likelihood function to a series of interpretable univariate functions. These univariate results then provide insight into the curvature of the log-likelihood function, and hence the uncertainty in the MLE point estimates. The resulting univariate function results in what is known as the *profile log-likelihood function* [31]. Following [15, 33, 40], we define the profile log-likelihood in terms of the interest parameter $D\lambda$. For a given value of $D\lambda$, we define the normalised profile log-likelihood:

$$\ell_p(D\lambda) = \max_{\lambda \in \Lambda} \left[\ell(D\lambda, \lambda) \right] - \ell^*, \tag{8}$$

where $\ell(D\lambda, \lambda) = \ell(\boldsymbol{\theta})$, $\ell^* = \ell(\hat{\boldsymbol{\theta}})$, and $\Lambda = \{\lambda : 0\,\text{day}^{-1} < \lambda \leqslant 5\,\text{day}^{-1}\}$. This definition gives a simple univariate function of $D\lambda$ that reaches a maximum of zero at the MLE, and the curvature of this function is related to inferential precision — a profile log-likelihood function with a well-defined peak at zero indicates a parameter that has been well estimated and identified, while a flat profile means that the data was insufficient for estimating or obtaining any inference for that parameter [40, 45]. A useful feature of (8) is that it can be used for constructing approximate confidence intervals for $D\lambda$, with an approximate $100(1 - \alpha)\%$ confidence interval given by the set of all $D\lambda$ such that $\ell_p(D\lambda) \geqslant -\chi^2_{1,1-\alpha}/2$ [31]. In this work, we use $\alpha = 0.05$ so that we are constructing 95% confidence intervals, giving $c^* = -\chi^2_{1,0.95}/2 \approx -1.92$. The procedure we use for computing profile likelihoods is implemented in the Julia package `ProfileLikelihood.jl` [46], and a summary of the procedure is outlined in Section S5 of the Supplementary Material.

2.4.4. Parameter-wise prediction intervals

The two-dimensional likelihood function allows us to propagate the uncertainty in $D\lambda$ through to give us a prediction interval in terms of the outcome of the mathematical model for a variable of interest, such as the bridging time or cell density. Using the approach developed by [33, 40] which builds on basic properties of likelihood function [31], we are able to quantify the uncertainty in the cell densities $u(x, y, t)$ and the bridging time t_b directly from our likelihood function. In particular, by taking pairs of parameter values inside of the 95% credible region from the log-likelihood function and computing the variable of interest at each pair, we obtain a sample of values that gives the uncertainty in our variable of interest, as described in Section S5 of the Supplementary Material. We use this method to obtain prediction intervals for $y_c^{i,j}$ and $y_p^{i,j}$ over time. Moreover, we can obtain prediction intervals for the bridging time, t_b, at which $\mu_c(t)$ first becomes zero. This procedure returns, in addition to the prediction intervals, a sample of bridging times, which we use to obtain probability distributions for the bridging time via `KernelDensity.jl` [47]. We represent this probability distribution using a probability density function (PDF) $p(t_b)$ for the bridging time which can be understood as [42]

$$p(t_b)\Delta t \approx \mathbb{P}(t < t_b < t + \Delta t), \tag{9}$$

where $\mathbb{P}(t < t_b < t + \Delta t)$ is the probability that the bridging time t_b is between t and $t + \Delta t$, given the uncertainty in the parameters $\boldsymbol{\theta}$, and Δt is some small sufficiently interval of time. This PDF $p(t_b)$ allows us to compute probabilities that the bridging time occurs in *any* given interval. The complete procedure for how we obtain these results is implemented

9

in `ProfileLikelihood.jl` [46], and the method that we implement is outlined in Section S5 of the Supplementary Material.

2.4.5. Predicting variability in tissue growth

We further extend our results to provide a more qualitative approach to assess the uncertainty in the tissue growth on these pores. Taking values for the parameters inside their confidence intervals from the profile likelihoods, we can produce time series model predictions of the solution to Equations (2)–(4), indicating the variability that we might expect in the tissue growth. For these predictions, we take three parameter values for θ: (1) $\hat{\theta}$, the MLE; (2) $\hat{\theta}_L$, where we take $D\lambda$ to be the lower endpoint of its confidence interval from $\ell_p(D\lambda)$ and λ to be the lower endpoint of its confidence interval from $\ell_p(\lambda)$; (3) $\hat{\theta}_U$, where we take $D\lambda$ to be the upper endpoint of its confidence interval from $\ell_p(D\lambda)$ and λ to be the upper endpoint of its confidence interval from $\ell_p(\lambda)$. Solving Equations (2)–(4) with these three combinations of θ provides a simple way of giving a visual interpretation of the uncertainty in cell density as an approximation to the true uncertainty bounds.

3. Results

We now give the results from our experiments and from our likelihood analysis. Following these results, we conclude with a description of how we can use these results to predict future pore bridging experiments.

3.1. Experimental images

A subset of the results for the pore bridging experiments on the square geometry are shown in Figure 3 for days 7, 14, 25, and 28, where we see most of the pores take longer than 14 days to bridge, although there is some significant variability in this bridging time as we can even see some pores have completely bridged by day 14. In each pore, the growing tissue always forms a circle before bridging. In total, we have $n = 41$ imaged pores included in the dataset for the square, with 26 at day 7 and 15 at day 14.

The results we use for the pore bridging experiments on the wave geometry come only from day 14, and they are shown in Figure 4. Just as we saw in Figure 3, there is significant variability in the bridging time – while most pores appear to have bridged by day 14, some are still open, with a few being far from closed. In these wave pores, the void appears to initially close in as an oval before the void boundary eventually forms a circle. Our interest is in comparing the cell migration and cell proliferation rates between the pores of Figure 3 and Figure 4, but from these images it is not immediately clear whether these are similar or not. Section 3.2 shows results making this comparison using a mathematical model. In total, we only have $n = 3$ pore images for the wave geometry, all at day 14, since all other pores are closed and thus no other data is available for $y_c^{i,j}$ and $y_p^{i,j}$, or parts of the scaffolds were not imaged as in the leftmost pore in the first image of Figure 4. The pores used for the data are given in the first, fourth, and sixth images in Figure 4.
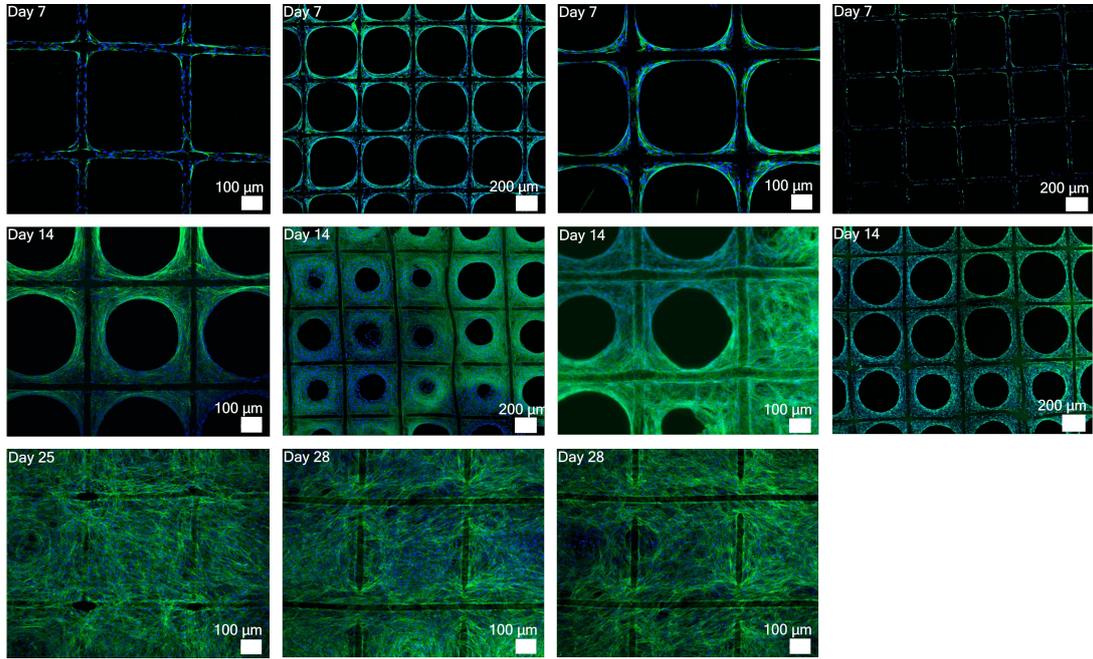
Figure 3: Experimental images for the square geometry. The images are composite fluoresence microscopy images of pore bridging experiments, with the blue channel showing the cell nuclei (stained with DAPI); the green channel showing the tissue and cytoskeleton (stained with phalloidin). Note that each image is from an independent experiment.
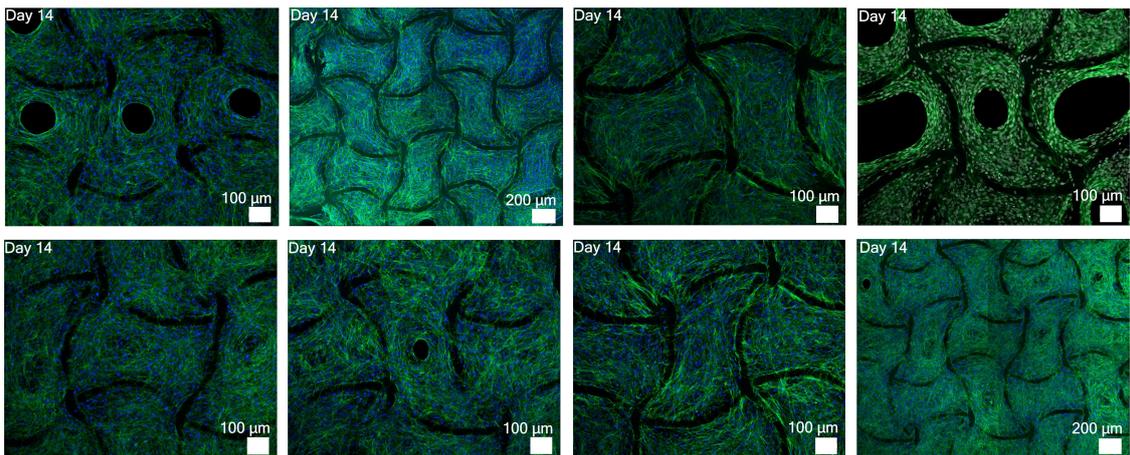

Figure 4: Experimental images for the wave geometry on day 14 of each experiment. The images are composite fluoresence microscopy images of pore bridging experiments, with the blue channel showing the cell nuclei (stained with DAPI); the green channel showing the tissue and cytoskeleton (stained with phalloidin). Note that each image is from an independent experiment.

3.2. Parameter estimation and parameter identifiability

We now consider the likelihoods, profile likelihoods, prediction intervals, and tissue growth predictions for the square and wave pores, demonstrating how well we can calibrate our model to the experimental data and make predictions between the two geometries.
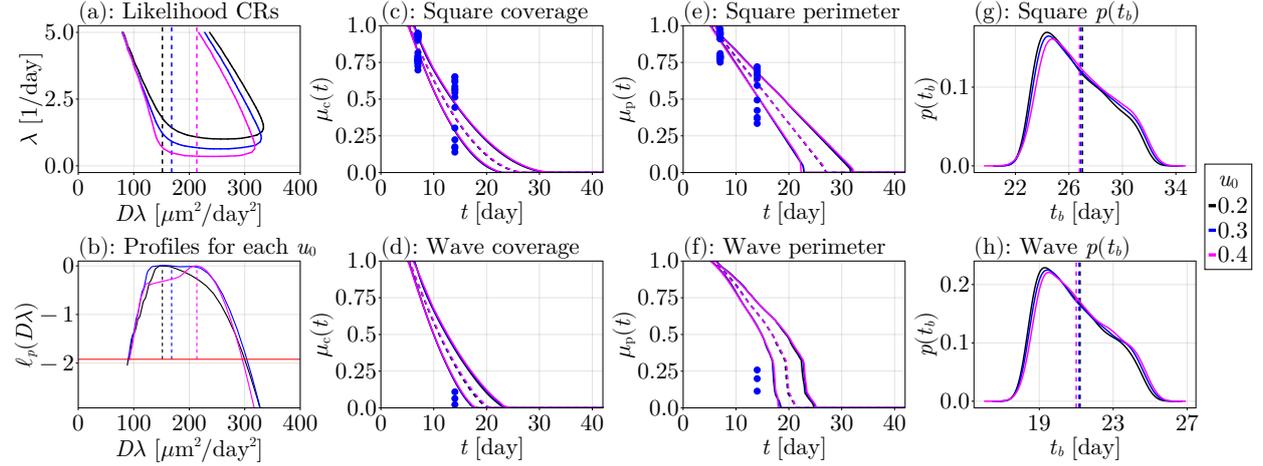
3.2.1. Square pore

Figure 5: Likelihood analysis results for the square pore. In (a), the lines give the boundaries of the 95% credible region for $\boldsymbol{\theta}$ for each u_0, and the vertical dashed lines show the MLE for $D\lambda$ (see Table 1). The profile log-likelihoods for $D\lambda$ for each u_0 are shown in (b), with the threshold $c^* \approx -1.92$ shown with a horizontal red line and the vertical dashed lines show the MLEs for $D\lambda$. In (c)–(f), predictions for $\mu_c(t)$ and $\mu_p(t)$ on each pore geometry are shown, with the blue dots showing the experimental data, the surrounding solid lines giving 95% prediction intervals for each u_0, and the dashed lines showing the corresponding estimates at the MLE $\hat{\boldsymbol{\theta}}$. The estimates for the PDF $p(t_b)$ of the bridging time on each pore geometry are shown in (g)–(h). The results in (d), (f), and (h) are predictions on the wave geometry using parameters inferred from the square pore data.

Figure 5(a) shows that the credible regions for $(D\lambda, \lambda)$ for each u_0 have a similar shape, and the MLEs for $D\lambda$ are all around the same value. The boundary of each credible region is well-defined in $D\lambda$ but not for λ, indicating that we are only able to obtain reliable estimates for $D\lambda$ but not for λ as we might anticipate [16, 37]. The confidence intervals we obtain from the profile log-likelihoods shown in Figure 5(b) for $D\lambda$ are approximately the same for each u_0, given approximately by $90\,\mu\text{m}^2/\text{day}^2 < D\lambda < 300\,\mu\text{m}^2/\text{day}^2$ for each u_0. The width of this interval is relatively small, noting that previously reported estimates of D in the literature vary across several orders of magnitude [15, 48]. The predictions for $\mu_c(t)$ on each geometry are shown in Figure 5(c)–(d). We see in (c) that we can recover the data on the square, with the prediction intervals capturing the average experimental data points, and the prediction intervals are indistinguishable for each u_0. The dashed lines show the predictions from the MLE $\hat{\boldsymbol{\theta}}$, indicating the most likely outcome of the experiments, and these curves too pass through the average of the experimental data points and are indistinguishable for each u_0. In contrast, we see for $\mu_c(t)$ on the wave geometry that we do not capture the precise values for $y_c^{i,j}$, although if we had more data points then we would likely capture more values due to their variability. These results are also independent for u_0. The corresponding figures for $\mu_p(t)$ are shown in Figure 5(e)–(f), where we again capture the data on the square pore but not the data from the wave pore, and again the curves are all independent

12

of u_0. Lastly, we show the probability distributions for the bridging time (9) on each pore geometry in Figure 5(g)–(h). These distributions have a similar shape for each u_0. The mode for t_b on the square pore appears to be around $t_b \approx 24$ days, and the distribution shows that we expect more pores to bridge between 23 to 30 days, consistent with our experiments in Figure 3. Similarly, the mode for t_b is around 20 days on the wave geometry, with most pores bridging within 19 to 24 days. The observation that the computed results in Figure 5, and in Figures 6–10, are all indistinguishable for each u_0 is an important result – it suggests that both the mean and variability in our estimates are relatively insensitive to u_0, indicating that precise measurements of u_0 are not critical.
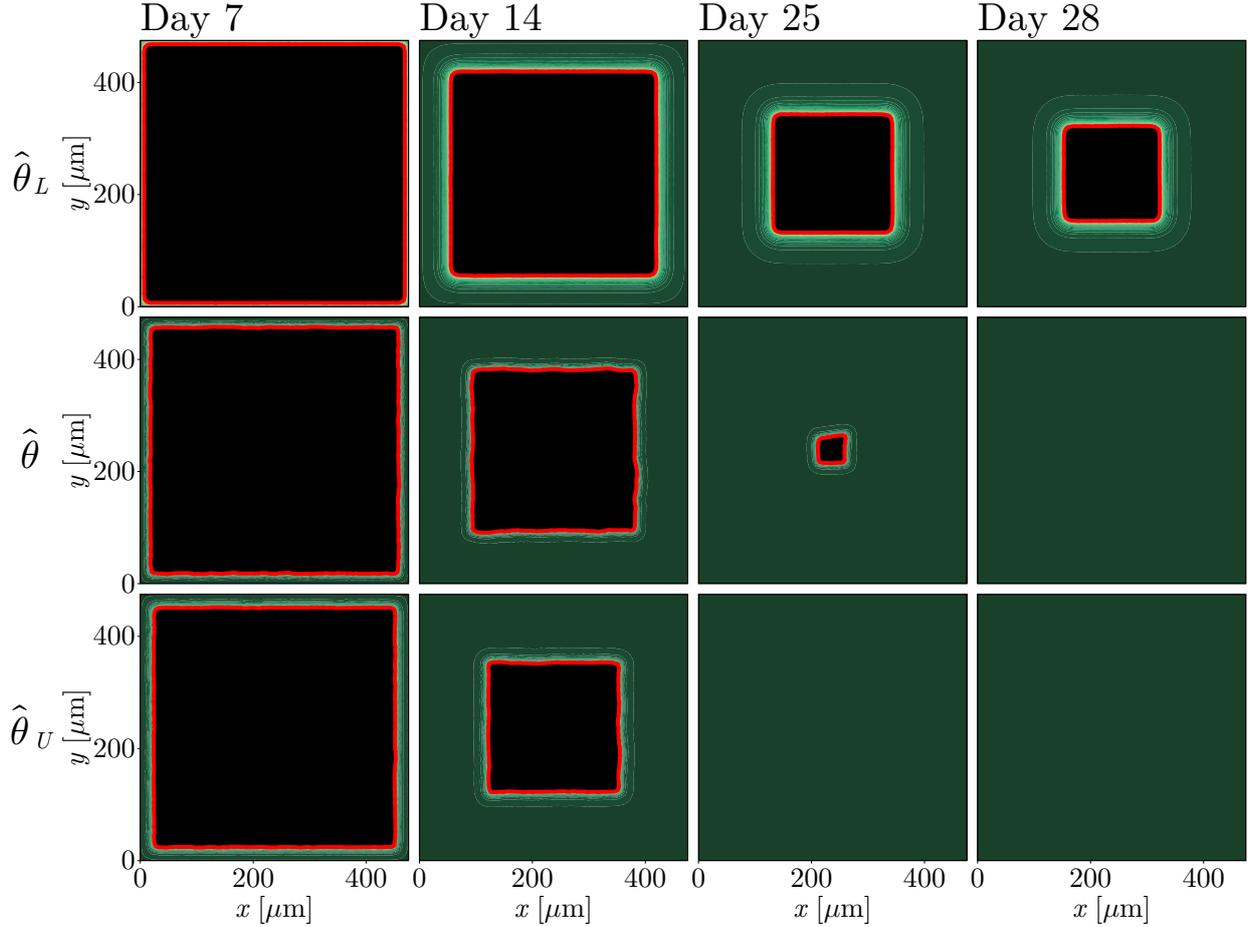

Figure 6: Model predictions for the variability in the tissue growth behaviour for the square geometry for $u_0 = 0.2$ at days 7, 14, 25, and 28. The parameters used are $\hat{\theta}_L = (\hat{D}_L, \hat{\lambda}_L) = (73\,\mu\mathrm{m}^2/\mathrm{day}, 1.2\,\mathrm{day}^{-1})$, $\hat{\theta} = (\hat{D}, \hat{\lambda}) = (32\,\mu\mathrm{m}^2/\mathrm{day}, 4.9\,\mathrm{day}^{-1})$, and $\hat{\theta}_L = (\hat{D}_U, \hat{\lambda}_U) = (60\,\mu\mathrm{m}^2/\mathrm{day}, 5\,\mathrm{day}^{-1})$.

Figure 6 shows a summary of model predictions where we explore the variability in the behaviour of the experiments over time. In particular, we show numerical solutions of Equations (2)–(4) at $\hat{\theta}$, $\hat{\theta}_L$, and $\hat{\theta}_U$, each for $u_0 = 0.2$. In this figure, the columns show predictions for a given time, with each row corresponding to a different value for θ. The middle row corresponds to $\hat{\theta}$, meaning the prediction that we expect to be most likely. The first two columns show model predictions for the two days that we use for calibrating the model, while the last two columns are genuine

predictions since our mathematical model is not calibrated to data from these predictions. We see that there is a lot of variability in the position of the void boundary, especially at day 14, depending on the choice of $\hat{\boldsymbol{\theta}}_L$, $\hat{\boldsymbol{\theta}}$, or $\hat{\boldsymbol{\theta}}_U$, which approximately matches the observed variability in the experimental images in Figure 3. The numerical results on day 14 show that, at $\boldsymbol{\theta} = \hat{\boldsymbol{\theta}}_L$, the void boundary is still close to the pore boundary, but the bottom row shows that, at $\boldsymbol{\theta} = \hat{\boldsymbol{\theta}}_U$, the pore is half-way to being filled. The tissue boundaries do not round off as clearly as in Figure 3, although there is some rounding in the corners of these boundaries; this is a limitation of how we calibrate our model, where we are instead seeing results averaged over more shapes. For some simulations in between the limits of the confidence intervals, the tissue boundary rounds off more strongly (not shown).
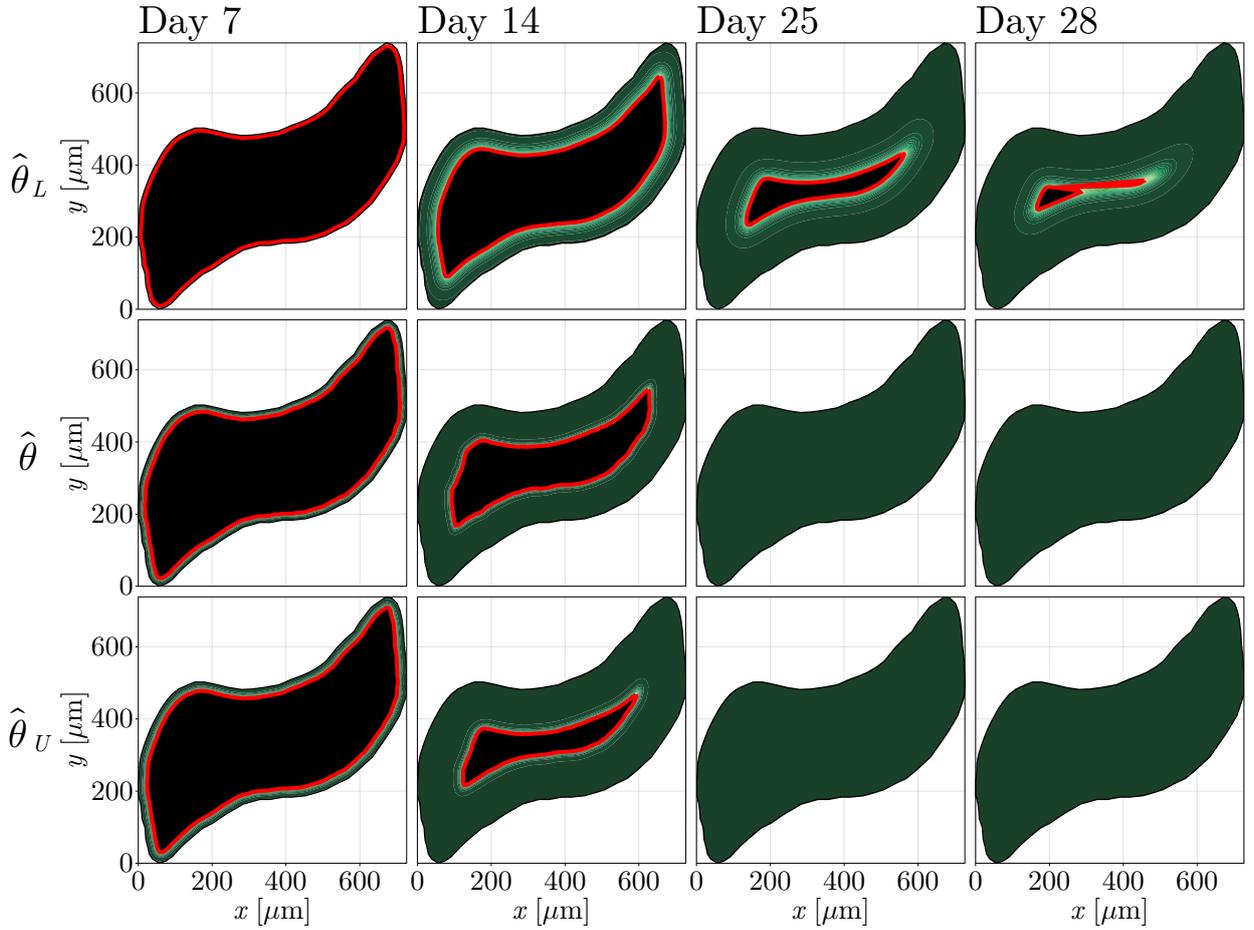

Figure 7: Model predictions for the variability in the tissue growth behaviour for the wave geometry using results from the square geometry for $u_0 = 0.2$ at days 7, 14, 25, and 28. The parameters used are $\hat{\boldsymbol{\theta}}_L = (\hat{D}_L, \hat{\lambda}_L) = (73\,\mu\text{m}^2/\text{day}, 1.2\,\text{day}^{-1})$, $\hat{\boldsymbol{\theta}} = (\hat{D}, \hat{\lambda}) = (32\,\mu\text{m}^2/\text{day}, 4.9\,\text{day}^{-1})$, and $\hat{\boldsymbol{\theta}}_L = (\hat{D}_U, \hat{\lambda}_U) = (60\,\mu\text{m}^2/\text{day}, 5\,\text{day}^{-1})$.

The model predictions of the tissue growth in Figure 7 show predictions of how the wave pores will evolve over time for $u_0 = 0.2$, using parameter estimates obtained by calibrating Equations (2)–(4) to data from the square pores. Similar to what we noted in Figure 6, we do not see the same circular voids in Figure 7 as we do in the experimental images in Figure 4, though this is expected as the predictions average over many curves. Similarly, we see high

variability in the results, with pores at day 14 ranging from being slightly closed to more than half-way closed. This variability is a positive result, matching the variability in the experimental images (Figure 4).

Together, these model predictions indicate that our model has been well-calibrated to the experimental data on the square pore, as we have captured the experimental data with our predictions and computed sensible probability distributions for the bridging time. The model predictions applied to the wave pore are reasonable, giving evidence of the similarities between the cell migration and cell proliferation mechanisms between the two geometries, although this is difficult to assess with few data points. Section 3.2.2 discusses the analogous results where we instead consider the model predictions from the experimental data on the wave.
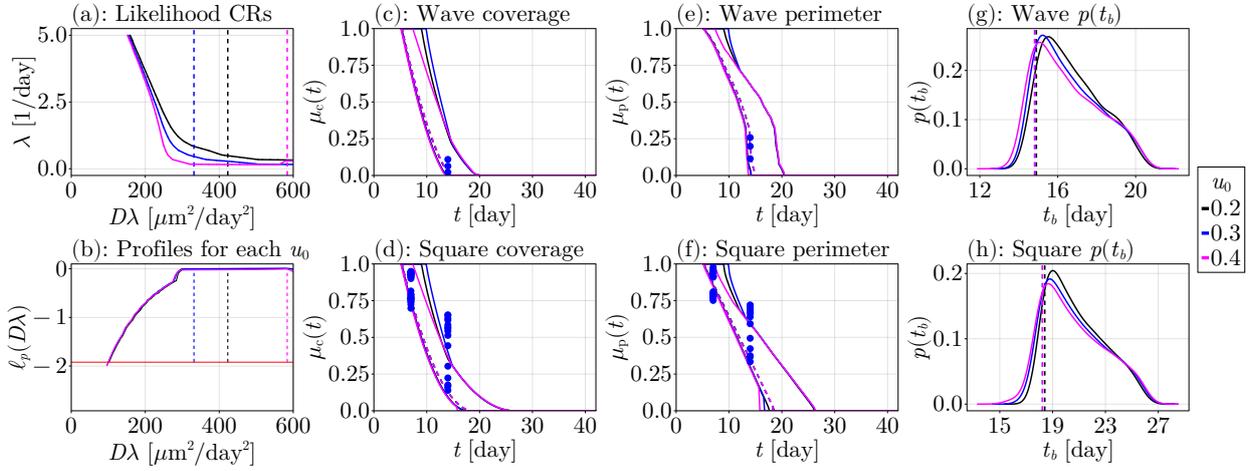
3.2.2. *Wave-like pore*

Figure 8: Likelihood analysis results for the wave pore. In (a), the lines give the boundaries of the 95% credible region for θ for each u_0, and the vertical dashed lines show the MLE for $D\lambda$ (see Table 1). The profile log-likelihoods for $D\lambda$ for each u_0 are shown in (b), with the threshold $c^* \approx -1.92$ shown with a horizontal red line and the vertical dashed lines show the MLEs for $D\lambda$. In (c)–(f), predictions for $\mu_c(t)$ and $\mu_p(t)$ on each pore geometry are shown, with the blue dots showing the experimental data, the surrounding solid lines giving 95% prediction intervals for each u_0, and the dashed lines showing the corresponding estimates at the MLE $\hat{\theta}$. The estimates for the PDF $p(t_b)$ of the bridging time on each pore geometry are shown in (g)–(h). The results in (d), (f), and (h) are predictions on the square geometry using parameters inferred from the wave pore data.

We now show the results obtained when we instead estimate $D\lambda$ from the data on the wave pore. The results have greater uncertainty here than in the square case since we have far fewer data points and only one day is covered by the data. The credible regions in Figure 8(a) are much wider and flatter at the bottom than they were in the square case (Figure 5(a)), meaning the estimates for $D\lambda$ are less precise. The credible region is not well-defined for larger values of $D\lambda$, indicating that we are unable to give any estimate for an upper bound on $D\lambda$. The corresponding profile log-likelihoods in Figure 8(b) for each u_0 do not intersect the threshold $c^* \approx -1.92$, independently of u_0, and so we are unable to give any estimate for the upper limit of the confidence intervals for $D\lambda$, as was already suggested from Figure 8(a). Despite these difficulties, Figures 8(c)–(f) suggest that we are able to recover values for the experimental data $y_c^{i,j}$ and $y_p^{i,j}$ on each pore geometry, with the predictions from the MLEs going through the experimental data points on each geometry. The probability distribution for the bridging time for the wave pore is shown in Figure 8(g),

where we see a mode for t_b around 14 days, with most pores predicted to close between 10 and 18 days, which is consistent with Figure 4. The corresponding probability distribution for the square geometry is shown in Figure 8(h), where we see that most pores are expected to close between 15 and 25 days, which is a shift from Figure 5(g) but is still consistent with the experimental images in Figure 3. It is important to emphasise that the recovery of these results on the square pore with so few data points is remarkable, as it (1) demonstrates the similarity between the migration and proliferation mechanisms on the two geometries, providing further evidence for the first research question, and (2) shows that we do not need such detailed, or even plentiful, data to recover these cellular mechanisms from another geometry.
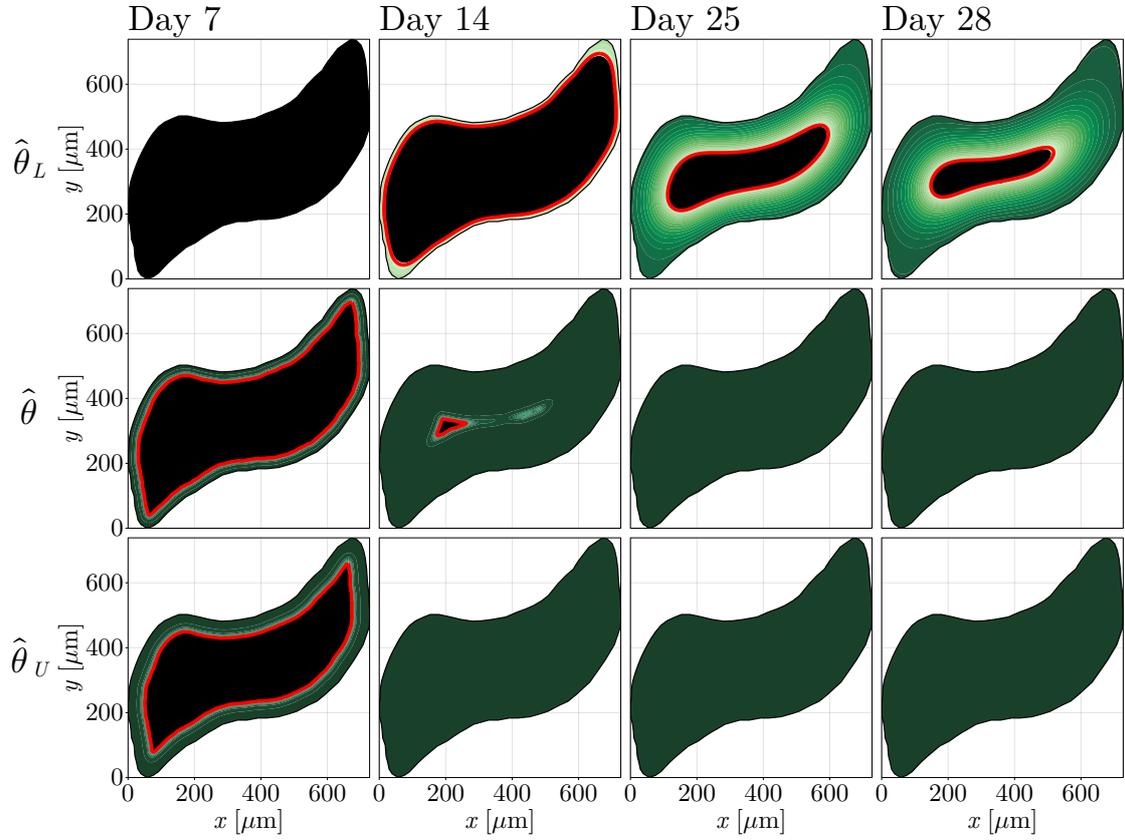

Figure 9: Model predictions for the variability in the tissue growth behaviour for the wave geometry for $u_0 \in \{0.1, 0.2, 0.3, 0.4\}$ at days 5, 7, 14, 25, and 28. The parameters used are $\hat{\boldsymbol{\theta}}_L = (\hat{D}_L, \hat{\lambda}_L) = (581 \, \mu\text{m}^2/\text{day}, 0.18 \, \text{day}^{-1})$, $\hat{\boldsymbol{\theta}} = (\hat{D}, \hat{\lambda}) = (58 \, \mu\text{m}^2/\text{day}, 7.29 \, \text{day}^{-1})$, and $\hat{\boldsymbol{\theta}}_L = (\hat{D}_U, \hat{\lambda}_U) = (117 \, \mu\text{m}^2/\text{day}, 10 \, \text{day}^{-1})$.

Predictions of tissue growth for the wave geometry, based on experimental data on the wave geometry, are shown in Figure 9 for $u_0 = 0.2$. These model simulations are consistent with our experimental observations in Figure 4. The middle row, displaying the most likely outcome, shows that essentially all pores will be closed by 14, which matches Figure 4. The model simulations at day 14 show that while some pores may be completely open at this time, some may be closed or almost closed, and we expect this significant variability as we have so few data points.

The predictions we make for the tissue growth on the square geometry using model results on the wave pore are
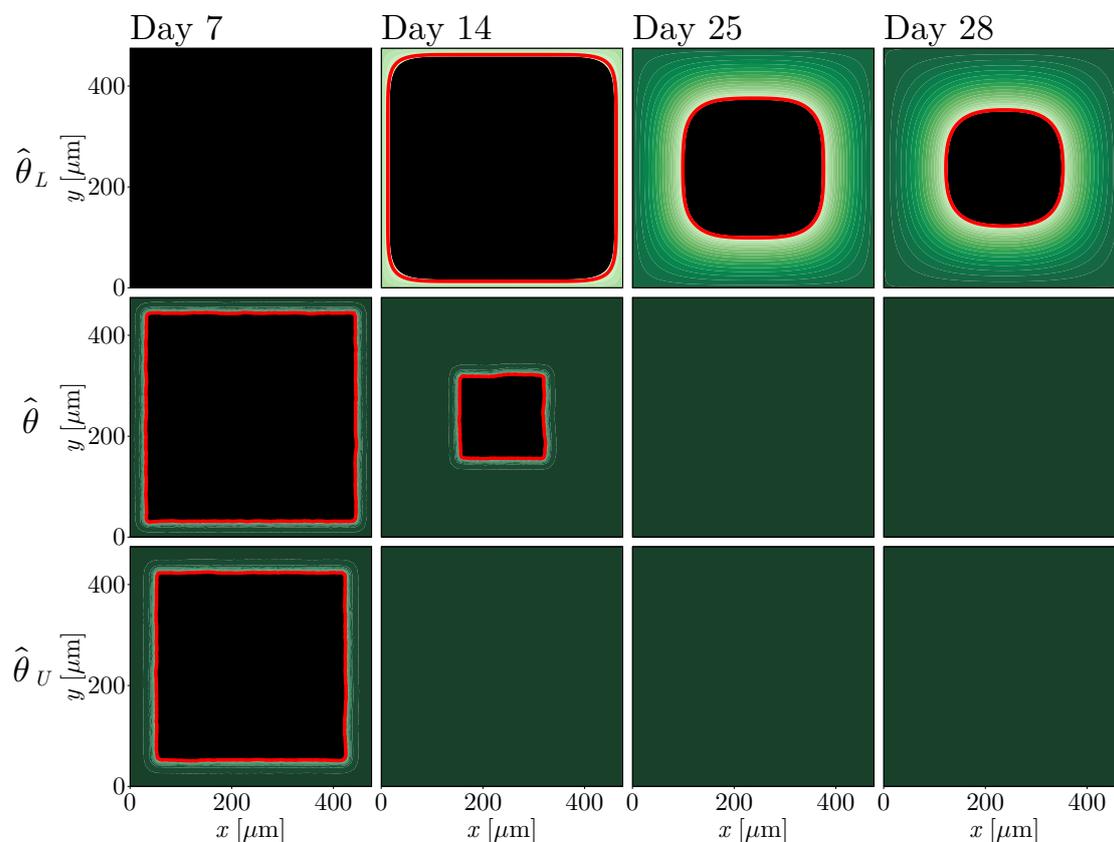
Figure 10: Model predictions for the variability in the tissue growth behaviour for the square geometry using results from the wave geometry for $u_0 = 0.2$ at days 7, 14, 25, and 28. The parameters used are $\hat{\boldsymbol{\theta}}_L = (\hat{D}_L, \hat{\lambda}_L) = (581\,\mu\text{m}^2/\text{day}, 0.18\,\text{day}^{-1})$, $\hat{\boldsymbol{\theta}} = (\hat{D}, \hat{\lambda}) = (58\,\mu\text{m}^2/\text{day}, 7.29\,\text{day}^{-1})$, and $\hat{\boldsymbol{\theta}}_L = (\hat{D}_U, \hat{\lambda}_U) = (117\,\mu\text{m}^2/\text{day}, 10\,\text{day}^{-1})$.

given in Figure 10. We observe significant variations in the closing time. In particular, while there could be some pores that are only halfway bridged by day 25 or day 28, most are close to closing by day 14 and completely closed by day 25, consistent with Figure 3. The middle row shows that the most likely outcome, according to our model, is that the majority of pores will be halfway bridged at day 14 and closed by day 25, which again matches Figure 3.

Overall, these model predictions indicate that, despite only having three data points, we have been able to calibrate our mathematical model sufficiently well so that we capture the original experimental data on the wave from our model predictions and, most importantly, we can recover the experimental data from the square pore from our experimental data on the wave pores. Moreover, the estimated probability distributions for the bridging times on each geometry are a good match to the experimental images in Figures 3–4, as are the predictions of the tissue growth from the model simulations. Thus, not only have we demonstrated the practicality and utility of our method for obtaining these probability distributions, we have provided much stronger evidence than in Section 3.2.1 that the cellular mechanisms driving tissue growth are similar between the two geometries.

3.2.3. Tabulated comparison between the two geometries

Table 1 compares values of $D\lambda$ and t_b, for $u_0 = 0.2$, for the two geometries; the choice of $u_0 = 0.2$ is not significant as the model results are relatively insensitive to this choice. We see that, while we cannot estimate the upper limit of the confidence interval for $D\lambda$ using the wave geometry, the lower limits are similar between the two geometries, as are the MLEs. Note that while the MLEs differ by a factor of three, this is an insignificant amount when we note that estimates for D could vary by many orders of magnitude [15]. These values for $D\lambda$ provide strong evidence that the cellular mechanisms driving tissue growth on the two geometries are the same. The estimates of the bridging times for each geometry are not too dissimilar when using either the same geometry or predicting from the other geometry.

	Square		Wave	
	MLE	95% CI	MLE	95% CI
$D\lambda$ [μm^2/day^2]	152	$(90, 299)$	423	$(107, -)$
t_b (square) [day]	27	$(24, 31)$	19	$(15, 22)$
t_b (wave) [day]	21	$(19, 24)$	15	$(13, 18)$

Table 1: Estimates for $D\lambda$ and t_b on each geometry for $u_0 = 0.2$. The 95% CI column gives the 95% confidence interval for the respective quantities, and the *MLE* column shows the corresponding MLEs. The second row gives predictions of the bridging time on the square geometry, while the third row is for the bridging time on the wave geometry.

Overall, these model results support the hypothesis that the cellular mechanisms driving the tissue growth on each geometry are similar. Moreover, the ability to calculate reasonable estimates and probability distributions for the bridging time provides evidence that the results obtained from one geometry can be used to make predictions about tissue growth on another geometry using the available data.

3.3. Prediction of tissue growth on a hypothetical geometry

We now take the results on the square geometry and use them to make predictions on a new geometry that is yet to be experimentally tested. The purpose of this exercise is to demonstrate how our mathematical modelling tools could be used for making predictions on a new geometry from experimental results on a simpler geometry, such as about bridging times, without having to conduct any (potentially expensive and time-consuming) experiments. The geometry we consider is a cross-shaped pore. Using the same values for $D\lambda$ as were used in making the predictions in Figures 6 and 7, we produce the model predictions for the variability in the tissue growth in this new geometry in Figure 11. We see a similar variance in the previous predictions, namely most pores are closed by day 25 but at $\hat{\theta}_L$ there are still some pores that remain half closed. The void maintains the symmetry of the geometry, forming a diamond shape during the early part of the growth process. These results are also largely independent of u_0, as we find when plotting these predictions for other u_0 values (not shown). We similarly show predictions for the $y_c^{i,j}$ and $y_p^{i,j}$ in Figure 12(a)–(b) and the hypothetical bridging time distribution $p(t_b)$ in Figure 12(c), all for $u_0 = 0.2$

An important feature of working with these predictions is that, once the likelihood results have been obtained, producing these predictions in Figures 11–12, or for any new geometry, is not a significantly time consuming task. The snapshots in Figure 11 take only around a minute to compute and visualise, and the model predictions in Figure

[12](#) may take around 10 minutes to an hour, depending on the number of samples requested for the prediction intervals. Thus, this type of exploratory analysis of a new geometry can be efficiently performed in a reasonable time.
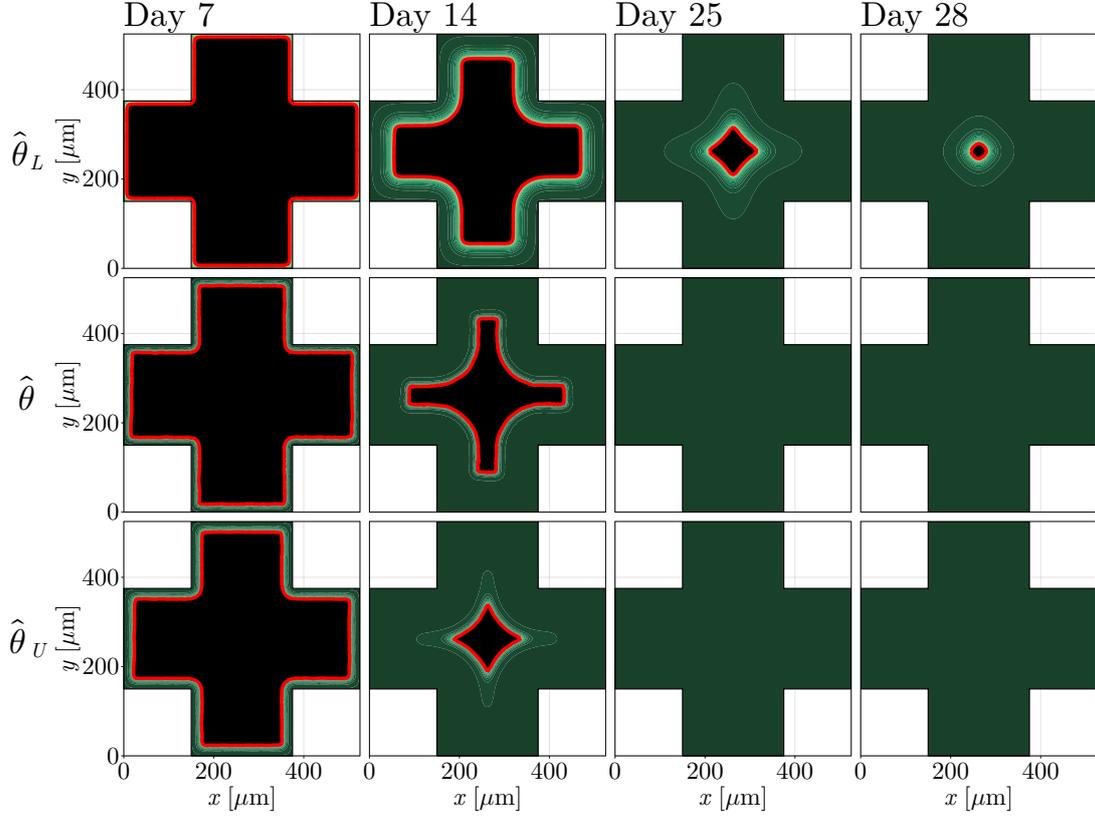

Figure 11: Model predictions for the variability in the tissue growth behaviour for the hypothetical geometry using results from the square geometry for $u_0 = 0.2$ at days 7, 14, 25, and 28. The parameters used are $\hat{\boldsymbol{\theta}}_L = (\hat{D}_L, \hat{\lambda}_L) = (73\,\mu\mathrm{m}^2/\mathrm{day}, 1.2\,\mathrm{day}^{-1})$, $\hat{\boldsymbol{\theta}} = (\hat{D}, \hat{\lambda}) = (32\,\mu\mathrm{m}^2/\mathrm{day}, 4.9\,\mathrm{day}^{-1})$, and $\hat{\boldsymbol{\theta}}_L = (\hat{D}_U, \hat{\lambda}_U) = (60\,\mu\mathrm{m}^2/\mathrm{day}, 5\,\mathrm{day}^{-1})$.
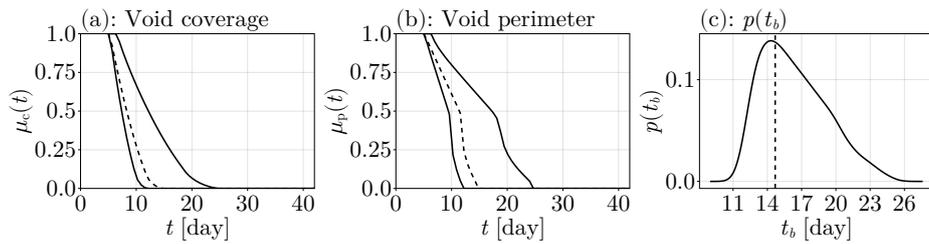

Figure 12: Predictions for the summary statistics and bridging distributions on the hypothetical geometry using results from the square geometry in Figure [5](#) at $u_0 = 0.2$. In (a)–(b), the dashed lines show the estimated curve corresponding to the maximum likelihood estimate for $(D\lambda, \lambda)$ from the square pore, and the curves surrounding it define a 95% uncertainty band for the curve.

4. Discussion

New experimental images and modelling predictions in Section 3 provide answers to the three research questions posed in Section 1. The first question, namely whether the cellular mechanisms driving tissue growth are independent of pore shape, appears to be true for the geometries considered. The second question asks whether we can make predictions of bridging times, with uncertainty, on a geometry from a separate geometry. We have found that we can produce reliable predictions with uncertainty between separate geometries, both in the form of probability distributions and prediction intervals. The third question concerns the type and quantity of data required for making predictions between geometries. We found that the data, and the amount of data, we use for summarising the images is sufficient for making predictions of tissue growth with uncertainty, namely information about the tissue void — even with only three data points on the wave geometry. Interestingly, the answers to these questions require only very simple measurements of the experiments, rather than performing cell counting [49]. This observation agrees with previous work that has compared methods using leading edge detection and cell counting, demonstrating that tracking the leading edge is sufficient for estimating the cell migration and cell proliferation rates [49]. We show in Section S6 of the Supplementary Material that if we considered only void area for the analysis of the square geometry then we would obtain the same conclusions, but both area and perimeter are necessary for the wave geometry to answer the research questions. The fact that both area and perimeter are required in general can be expected since area and perimeter together give a detailed description of a shape, but not separately.

These answers have important implications. Firstly, we have demonstrated the ability to extrapolate from experimental results on one geometry to another geometry, making predictions with uncertainty. This facilitates fast and inexpensive pilot studies to be performed for new pore geometries without conducting the experiments or even fabricating the scaffolds, as with our exploratory analysis in Section 3.3. Numerical simulations could be performed in a few minutes of computation on a standard desktop computer, while conducting the necessary experiments will require more than one month for tissue growth and a considerable amount of effort and expense to fabricate the scaffolds with melt electrowriting. We do not mean to imply that these predictions can replace experimental verification, instead we view this suite of predictive tools as complementary screening tools that can be used to plan and interpret experiments efficiently. Secondly, the novel method we present for obtaining probability distributions for the bridging time provides a useful tool for meeting certain needs by helping us to understand the amount of time required for a tissue to form and bridge the pore, and also for understanding how long tissue growth needs to be incubated for in tissue engineering constructs. Together with the type of exploratory analysis demonstrated in Section 3.3, these probability distributions can help facilitate the construction of a geometry that is likely to bridge within some time window for certain clinical needs, and for determining how long an experiment should be run for.

The mathematical model we use in this study is relative simple as it involves just three parameters: D, λ, and u_0. A model that better incorporates other effects such as cell adhesion or the different phases of tissue growth, in particular the initial phase where cells move off the scaffold or the later phase where the pore is closing and cells overlap [28],

20

could be of interest to provide more biological insight. A key limitation of working with a more detailed mathematical model, however, would be the need to collect significantly more data so that the necessary additional parameters can be properly estimated [40, 45].

5. Conclusion and future work

In this study, we use a reaction-diffusion model together with a likelihood-based uncertainty quantification framework to study how pore geometry affects tissue growth, particularly in how we can make inference about tissue growth on complicated pore geometries using data from tissue growth on simpler square geometries, providing new tools for studying tissue growth with uncertainty and providing probability distributions for bridging times. We use data from pore bridging experiments to perform this analysis, considering a square geometry and a wave-like geometry.

Our combined experimental and mathematical modelling results suggest that the cell migration and cell proliferation mechanisms driving tissue growth appear to be independent of the pore geometry, giving evidence that observed curvature effects are due to space availability rather than cellular mechanisms. We can make predictions of the bridging time on a new geometry in the form of a probability density function, a powerful tool for understanding both quantitatively and qualitatively what may happen in a pore bridging experiment on a new geometry, including the estimation of probabilities of bridging times over a given time interval.

There are several avenues for future work based on our findings in this study. First, our computational tools can be applied to new pore bridging experiments involving different geometries or different cell lines since our methods are independent of these two features. Secondly, it would be of interest to collect more data across more time points to explore the extent to which additional parameters, such as D and λ separately, can be estimated [15]. If future works consider more than one variable, we note that it would not be feasible to work with the plots of the log-likelihood function as we have done, and instead the profile log-likelihood would be required to obtain uncertainty quantification. Thirdly, the ability to make predictions on new geometries can facilitate a systematic study of how bridging times depend on curvature, such as by defining a geometry that depends directly on a specified curvature and comparing the probability distributions over many curvatures. This would provide a plausible set of outcomes to be analysed prior to running full-scale experiments exploring these features.

The predictions made on geometries from data on a separate geometry can be useful for facilitating a pilot study for pore bridging experiments on the geometry, such as the geometry demonstrated in Figure 11 and Figure 12. It would be of interest to see how well these predictions can help with preparing and investing into future experiments, for example in estimating what time scales an experiment may need to be run for by assessing the uncertainty in the bridging times. All code and data to reproduce this work are available on GitHub at https://github.com/DanielVandH/PoreBridging.jl in the JULIA language [50].

References

[1] A Khademhosseini and R Langer. A decade of progress in tissue engineering. *Nature Protocols*, 11:1775–1781, 2016.

[2] MJ Lysaght and J Reyes. The growth of tissue engineering. *Tissue Engineering*, 7:485–493, 2004.

[3] A-V Do, B Khorsand, SM Geary, and AK Salem. 3D printing of scaffolds for tissue regeneration applications. *Advanced Healthcare Materials*, 4:1742–1762, 2018.

[4] DP Forrestal, TJ Klein, and MA Woodruff. Challenges in engineering large customized bone constructs. *Biotechnology and Bioengineering*, 114:1129–1139, 2016.

[5] CM Nelson, RP Jean, JL Tan, WF Liu, NJ Sniadecki, AA Spector, and CS Chen. Emergent patterns of growth controlled by multicellular form and mechanics. *Proceedings of the National Academy of Sciences of the United States of America*, 102:11594–11599, 2005.

[6] CM Bidan, KP Kommareddy, M Rumpler, P Kollmannsberger, YJM Bréchet, P Fratzi, and JWC Dunlop. How linear tension converts to curvature: Geometric control of bone tissue growth. *PLOS ONE*, 7:e36336, 2012.

[7] M Rumpler, A Woesz, JWC Dunlop, JT van Dongen, and P Fratzl. The effect of geometry on three-dimensional tissue growth. *Journal of the Royal Society Interface*, 5:1173–180, 2008.

[8] ST Johnston, JV Ross, BJ Binder, DLS McElwain, P Haridas, and MJ Simpson. Quantifying the effect of experimental design choices for *in vitro* scratch assays. *Journal of Theoretical Biology*, 400:19–31, 2016.

[9] PS Zieliński, PKR Gudeti, T Rikmanspoel, and MK Włodarczyk-Biegun. 3D printing of bio-instructive materials: Toward directing the cell. *Bioactive Materials*, 19:292–327, 2022.

[10] MP Mani, M Sadia, SK Jaganathan, AZ Khudzari, E Supriyanto, S Saidin, S Ramakrishna, AF Ismail, and AAM Faudzi. A review on 3D printing in tissue engineering applications. *Journal of Polymer Engineering*, 42:243–265, 2022.

[11] A Hrynevich, BS Elçi, JN Haigh, R McMaster, A Youssef, C Blum, T Blunk, G Hochleitner, J Groll, and PD Dalton. Dimension-based design of melt electrowritten scaffolds. *Small*, 22:1800232, 2018.

[12] NC Paxton, J Ren, MJ Ainsworth, AK Solanki, JR Jones, MC Allenby, MM Stevens, and MA Woodruff. Rheological characterization of biomaterials directs additive manufacturing of strontium-substituted bioactive glass/polycaprolactone microfibers. *Macromolecular Rapid Communications*, 40:1900019, 2019.

[13] K Dzobo, NE Thomford, DA Senthebane, H Shipange, A Rowe, C Dandara, M Pillay, and KSCM Motaung. Advances in regenerative medicine and tissue engineering: Innovation and transformation of medicine. *Stem Cells International*, 2018:2495848, 2018.

[14] SJ Hollister, CL Flanagan, DA Zopf, RJ Morrison, H Nasser, JJ Patel, E Ebramzadeh, SN Sangiorgio, MB Wheeler, and GE Green. Design control for clinical translation of 3D printed modular scaffolds. *Annals of Biomedical Engineering*, 43:774–786, 2015.

[15] AP Browning, OJ Maclaren, PR Buenzli, M Lanaro, M C Allenby, MA Woodruff, and MJ Simpson. Model-based data analysis of tissue growth in thin 3D printed scaffolds. *Journal of Theoretical Biology*, 528:110852, 2021.

[16] PR Buenzli, M Lanaro, CS Wong, MP McLaughlin, MC Allenby, MA Woodruff, and MJ Simpson. Cell proliferation and migration explain pore bridging dynamics in 3D printed scaffolds of different pore size. *Acta Biomaterialia*, 114:285–295, 2020.

[17] PF Egan, SJ Ferguson, and K Shea. Design of hierarchical three-dimensional printed scaffolds considering mechanical and biological factors for bone tissue engineering. *Journal of Mechanical Design*, 139:061401, 2017.

[18] M Paris, A Götz, I Hettrich, CM Bidan, JWC Dunlop, H Razi, I Zizak, DW Hutmacher, P Fratzl, GN Buda, W Wagermaier, and A Ciptria. Scaffold curvature-mediated novel biomineralization process originates a continuous soft tissue-to-bone interface. *Acta Biomaterialia*, 60: 64–80, 2017.

[19] SJP Callens, RJC Uyttendaele, LE Fratila-Apachitei, and AA Zadpoor. Substrate curvature as a cue to guide spatiotemporal cell and tissue organization. *Biomaterials*, 232:119739, 2020.

[20] CM Bidan, KP Kommareddy, M Rumpler, P Kollmannsberger, P Fratzl, and JWC Dunlop. Geometry as a factor for tissue growth: Towards shape optimization of tissue engineering scaffolds. *Advanced Healthcare Materials*, 2:186–194, 2012.

[21] SJP Callens, D Fan, IAJ van Hengel, M Minneboo, PJ Díaz-Payno, MM Stevens, LE Fratila-Apachitei, and AA Zadpoor. Emergent collective organization of bone cells in complex curvature fields. *Nature Communicatons*, page 855, 2023.

[22] MA Alias and PR Buenzli. Osteoblasts infill irregular pores under curvature and porosity controls: a hypothesis-testing analysis of cell behaviours. *Biomechanics and Modeling in Mechanobiology*, 17:1357–1371, 2018.

[23] MA Alias and PR Buenzli. Modeling the effect of curvature on the collective behavior of cells growing new tissue. *Biophysical Journal*, 112: 193–204, 2017.

[24] MA Alias and PR Buenzli. A level-set method for the evolution of cells and tissue during curvature-controlled growth. *International Journal for Numerical Methods in Biomedical Engineering*, 36:e3279, 2019.

[25] SGD Hegarty-Cremer, MJ Simpson, TL Andersen, and PR Buenzli. Modelling cell guidance and curvature control in evolving biological tissues. *Journal of Theoretical Biology*, 520:110658, 2021.

[26] M Lanaro, MP Mclaughlin, MJ Simpson, PR Buenzli, CS Wong, MC Allenby, and MA Woodruff. A quantitative analysis of cell bridging kinetics on a scaffold using computer vision algorithms. *Acta Biomaterialia*, 136:429–440, 2021.

[27] W Jin, K-Y Lo, S-E Chou, SW McCue, and MJ Simpson. The role of initial geometry in experimental models of wound closing. *Chemical Engineering Science*, 179:221–226, 2018.

[28] PR Buenzli and MJ Simpson. Curvature dependences of wave propagation in reaction-diffusion models. *Proceedings of the Royal Society A*, 478:20220582, 2022.

[29] X-Z Yan, W Yang, F Yang, M Kersten-Niessen, JA Jansen, and SK Both. Effects of continuous passaging on minearlization of MC3T3-E1 cells with improved osteogenic culture protocol. *Tissue Engineering*, 20:198–204, 2014.

[30] JA Sherratt and JD Murray. Models of epidermal wound healing. *Proceedings of the Royal Society: Series B*, 241:29–36, 1990.

[31] Y Pawitan. *In All Likelihood: Statistical Modelling and Inference Using Likelihood*. Oxford University Press, Oxford, 2001.

[32] P Royston. Profile likelihood for estimation and confidence intervals. *The Stata Journal*, 7:376–387, 2007.

[33] MJ Simpson, SA Walker, EN Studerus, SW McCue, RJ Murphy, and OJ Maclaren. Profile likelihood-based parameter and predictive interval analysis guides model choice for ecological population dynamics. *Mathematical Biosciences*, 355:108950, 2023.

[34] AF Villaverde, N Tsiantis, and JR Banga. Full observability and estimation of unknown inputs, states and parameters of nonlinear biological models. *Journal of the Royal Society Interface*, 16:20190043, 2019.

[35] MJ Simpson. Depth-averaging errors in reactive transport modelling. *Water Resources Research*, 45:W02505, 2009.

[36] AP Browning, P Haridas, and MJ Simpson. A Bayesian sequential learning framework to parameterise continuum models of melanoma invasion into human skin. *Bulletin of Mathematical Biology*, 81:676–698, 2018.

[37] PK Maini, DLS McElwain, and DI Leavesley. Traveling wave model to interpret a wound-healing cell migration assay for human peritoneal mesothelial cells. *Tissue Engineering*, 10:475–482, 2004.

[38] KK Treloar and MJ Simpson. Sensitivity of edge detection methods for quantifying cell migration assays. *PLoS ONE*, 8:e67389, 2013.

[39] ST Vittadello, SW McCue, G Gunasingh, NK Hass, and MJ Simpson. Mathematical models for cell migration with real-time cell cycle dynamics. *Biophysical Journal*, 114:1241–1253, 2018.

[40] MJ Simpson and OJ Maclaren. A profile likelihood-based workflow for identifiability analysis, estimation, and prediction with mechanistic mathematical models. *bioRxiv*, 2023. doi: 10.1101/2022.12.14.520367.

[41] MJ Simpson, AP Browning, DJ Warne, OJ Maclaren, and RE Baker. Parameter identifiability and model selection for sigmoid population growth models. *Journal of Theoretical Biology*, 535:110998, 2022.

[42] G Casella and RL Berger. *Statistical Inference*. Duxbury, Pacific Grove, CA, 2 edition, 2002.

[43] L Wasserman. *All of Statistics: A Concise Course in Statistical Inference*. Springer Science & Business Media, New York, 2013.

[44] AP Browning, JA Sharp, RJ Murphy, G Gunasingh, B Lawson, K Burrage, NK Haass, and M Simpson. Quantitative analysis of tumour spheroid structure. *eLife*, 10:e73020, 2021.

[45] A Raue, C Kreutz, T Maiwald, U Klingmüller, and J Timmer. Addressing parameter identifiability by model-based experimentation. *IET Systems Biology*, 5:120–130, 2011.

[46] DJ VandenHeuvel. ProfileLikelihood.jl: Methods for profile likelihood analysis, April 2023. URL https://doi.org/10.5281/zenodo.7827704.

[47] S Byrne. KernelDensity.jl: Kernel density estimators for Julia. https://github.com/JuliaStats/KernelDensity.jl, 2014. Version 0.6.5.

[48] W Jin, ET Shah, CJ Penington, SW McCue, LK Chopin, and MJ Simpson. Reproducibility of scratch assays is affected by the initial degree of confluence: Experiments, modelling and model selection. *Journal of Theoretical Biology*, 390:136–145, 2016.

[49] KK Treloar, MJ Simpson, DLS McElwain, and RE Baker. Are in vitro estimates of cell diffusivity and cell proliferation rate sensitive to assay geometry? *Journal of Theoretical Biology*, 356:71–84, 2014.

[50] J Bezanson, A Edelman, S Karpinski, and VB Shah. Julia: A fresh approach to numerical computing. *SIAM Review*, 59:65–98, 2017.

[51] J Rokne. The area of a simple polygon. In J Arvo, editor, *Graphics Gems II*, pages 5–6. Morgan Kaufmann, San Diego, California, 1991.

[52] HK Versteeg and W Malalasekera. *An Introduction to Computational Fluid Dynamics*. Prentice Hall, Harlow, 2 edition, 2007.

[53] DJ VandenHeuvel. DelaunayTriangulation.jl: Delaunay triangulation and Voronoi tessellations of planar point sets, May 2023. URL https://doi.org/10.5281/zenodo.7964424.

[54] C. Rackauckas and Q. Nie. DifferentialEquations.jl — a performant and feature-rich ecosystem for solving differential equations in Julia. *Journal of Open Research Software*, 5:15, 2017.

[55] TA Davis and E Palamadai Natarajan. Algorithm 907: KLU, a direct sparse solver for circuit simulation problems. *ACM Transactions on Mathematical Software*, 37:1–17, 2010.

[56] ME Hosea and LF Shampine. Analysis and implementation of TR-BDF2. *Applied Numerical Mathematics*, 20:21–37, 1996.

[57] DJ VandenHeuvel. FiniteVolumeMethod.jl: Solver for two-dimensional conservation equations using the finite volume method, May 2023. URL https://doi.org/10.5281/zenodo.7950651.

[58] L Stagner. ConcaveHull.jl: Julia package for calculating 2D concave/convex hulls. https://github.com/lstagner/ConcaveHull.jl, 2017. Version 1.2.0.

[59] A Moreira and MY Santos. Concave hull: A *k*-nearest neighbours approach for the computation of the region occupied by a set of points. In J Braz, P.-P Vázquez, and J Madeiras Pereira, editors, *Proceedings of the 2nd International Conference on Computer Graphics Theory and Applications (GRAPP 2007)*, volume GM/R, pages 61–68. INSTICC - Institute for Systems and Technologies of Information, Control and Communication, march 2007. ISBN 978-972-8865-71-9.

[60] S. G. Johnson. NLopt.jl: Package to call the NLopt nonlinear-optimization library from the Julia language. https://github.com/JuliaOpt/NLopt.jl, 2013. Version 0.6.5.

[61] S. G. Johnson. The NLopt nonlinear-optimization package. https://github.com/stevengj/nlopt, 2010. Version 2.7.1.

[62] MJD Powell. The BOBYQA algorithm for bound constrained optimization without derivatives. Technical report, Department of Applied Mathematics and Theoretical Physics, Cambridge, England, 2009.

[63] R Boiger, J Hasenauer, S Hroß, and B Kaltenbacher. Integration based profile likelihood calculation for PDE constrained parameter estimation problems. *Inverse Problems*, 32:125009, 2016.

Appendix A. Summarising images from the experiments

Here we present the formulae for computing the area and perimeter summary statistics. As discussed in Section 2.2, for an image $I(t)$ at time t we identify a boundary $\mathcal{P}^I(t)$ for the pore and a boundary $\mathcal{V}^I(t)$ for the void. Precisely, we identify the sets $\mathcal{P}^I(t) = \{\mathbf{p}_1^I(t), \ldots, \mathbf{p}_n^I(t), \mathbf{p}_{n+1}^I(t)\}$ and $\mathcal{V}^I(t) = \{\mathbf{v}_1^I(t), \ldots, \mathbf{v}_m^I(t), \mathbf{v}_{m+1}^I(t)\}$, where $\mathbf{p}_{n+1}^I(t) = \mathbf{p}_1^I(t)$ and $\mathbf{v}_{m+1}^I(t) = \mathbf{v}_1^I(t)$ and the boundary points are arranged in counter-clockwise order. An example of these sets is shown in Figure A.13. Using these sets, the area of the pore and the area of the void for this image $I(t)$, denoted $A[\mathcal{P}^I(t)]$ and $A[\mathcal{V}^I(t)]$, respectively, can be computed [51]

$$A[\mathcal{P}^I(t)] = \frac{1}{2} \sum_{i=1}^{n} \det\left(\mathbf{p}_i^I(t), \mathbf{p}_{i+1}^I(t)\right) \quad \text{and} \quad A[\mathcal{V}^I(t)] = \frac{1}{2} \sum_{i=1}^{m} \det\left(\mathbf{v}_i^I(t), \mathbf{v}_{i+1}^I(t)\right). \tag{A.1}$$

Similarly, the perimeters $\ell[\mathcal{P}^I(t)]$ and $\ell[\mathcal{V}^I(t)]$ for the pore and void boundaries, respectively, are simply

$$\ell[\mathcal{P}^I(t)] = \sum_{i=1}^{n} \left\|\mathbf{p}_{i+1}^I(t) - \mathbf{p}_i^I(t)\right\| \quad \text{and} \quad \ell[\mathcal{V}^I(t)] = \sum_{i=1}^{n} \left\|\mathbf{v}_{i+1}^I(t) - \mathbf{v}_i^I(t)\right\|, \tag{A.2}$$

summing up each length like the one annotated in Figure A.13.
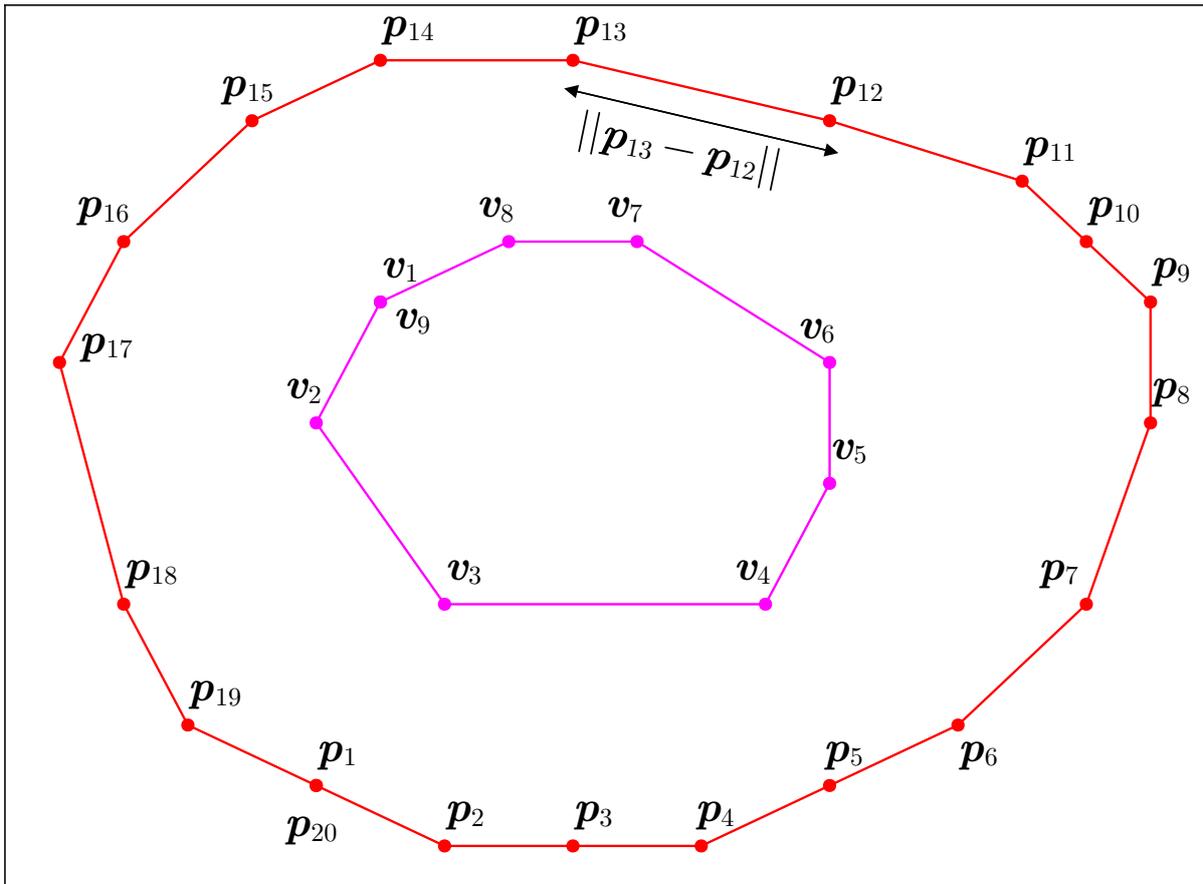
Figure A.13: Example of the configuration of the point sets $\mathcal{P}$ and $\mathcal{V}$, omitting the superscript I. These are $n = 19$ points on the pore boundary and $m = 8$ on the void boundary, with an extra point at the end of each set to close the boundary. Note also the order of the points.

Appendix B. Finite volume method

In this section, we give the details for how we solve the PDE

$$\frac{\partial u(\mathbf{x},t)}{\partial t} = D\boldsymbol{\nabla} \cdot [u(\mathbf{x},t)\boldsymbol{\nabla} u(\mathbf{x},t)] + \lambda u(\mathbf{x},t)(1 - u(\mathbf{x},t)), \quad \mathbf{x} \in \Omega, \tag{B.1}$$

$$\frac{\mathrm{d}u(\mathbf{x},t)}{\mathrm{d}t} = \lambda u(\mathbf{x},t)\,(1 - u(\mathbf{x},t))\,, \quad \mathbf{x} \in \partial\Omega, \tag{B.2}$$

$$u(\mathbf{x},t_a) = \begin{cases} u_0 & \mathbf{x} \in \partial\Omega, \\ 0 & \mathbf{x} \in \Omega, \end{cases} \tag{B.3}$$

using the finite volume method [52]. The first step is to compute a triangulation of the domain Ω, denoted $\mathcal{T}(\Omega)$, which we accomplish using `DelaunayTriangulation.jl` [53]. For some interior point $\mathbf{x}_i = (x_i, y_i)^\mathsf{T} \in \mathcal{T}(\Omega)$, we take the centroids of the triangles neighbouring $\mathbf{x}_i$ and connect these centroids to the midpoints of the associated triangle, giving a closed polygon that we denote by $\partial\Omega_i$ and show in Figure B.14. The interior of this polygon is denoted Ω_i, which we call a control volume, and has some volume V_i. This polygon is defined by a set of edges $\mathcal{E}_i$, and for each $\mathbf{x}_\sigma \in \mathcal{E}_i$ there is an associated length L_σ, midpoint $\mathbf{x}_\sigma$, and unit normal $\hat{\mathbf{n}}_{i,\sigma}$ which is normal to σ and directed outwards to Ω_i with unit length. It is with these control volumes that we can now discretise (B.1).
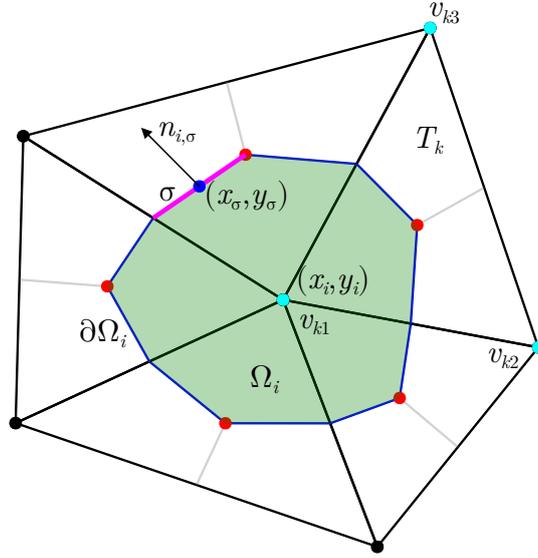

Figure B.14: Example of a control volume around a point $\mathbf{x}_i = (x_i, y_i)^\mathsf{T}$. The control volume is the region in green, and its boundary $\partial\Omega_i$ is shown in blue. The edge $\sigma \in \mathcal{E}_i$ is shown in magenta. Lastly, the cyan points show an example counter-clockwise ordering (v_{k1}, v_{k2}, v_{k3}) of a triangle $T_k \in \mathcal{T}(\Omega)$.

We integrate (B.1) over Ω_i,

$$\frac{\mathrm{d}}{\mathrm{d}t} \iint_{\Omega_i} u(\mathbf{x},t)\,\mathrm{d}A = D \iint_{\Omega_i} \boldsymbol{\nabla} \cdot [u(\mathbf{x},t)\boldsymbol{\nabla} u(\mathbf{x},t)]\,\mathrm{d}A + \lambda \iint_{\Omega_i} u(\mathbf{x},t)\,(1 - u(\mathbf{x},t))\,\mathrm{d}A\,. \tag{B.4}$$

The first integral on the right of (B.4) can be re-written as a line integral using the divergence theorem, and then re-written as a sum by integrating across each edge of $\partial\Omega_i$:

$$D \iint_{\Omega_i} \boldsymbol{\nabla} \cdot [u(\mathbf{x},t)\boldsymbol{\nabla} u(\mathbf{x},t)]\, \mathrm{d}A = D \oint_{\partial\Omega_i} [u(\mathbf{x},t)\boldsymbol{\nabla} u(\mathbf{x},t)] \cdot \hat{\mathbf{n}}_{i,\sigma}(\mathbf{x},t)\, \mathrm{d}s = D \sum_{\sigma \in \mathcal{E}_i} \int_{\sigma} [u(\mathbf{x},t)\boldsymbol{\nabla} u(\mathbf{x},t)] \cdot \hat{\mathbf{n}}_{i,\sigma}\, \mathrm{d}s, \quad \text{(B.5)}$$

with $\hat{\mathbf{n}}_i(\mathbf{x},t)$ the unit normal vector field on $\partial\Omega_i$. Next, defining the control volume averages

$$\bar{u}_i = \frac{1}{V_i} \iint_{\Omega_i} u(\mathbf{x},t)\, \mathrm{d}A \quad \text{and} \quad \bar{R}_i = \frac{\lambda}{V_i} \iint_{\Omega_i} u(\mathbf{x},t)\,(1 - u(\mathbf{x},t))\, \mathrm{d}A\,,$$

our integral formulation (B.4) becomes

$$\frac{\mathrm{d}\bar{u}_i}{\mathrm{d}t} = \frac{D}{V_i} \sum_{\sigma \in \mathcal{E}_i} \int_{\sigma} [u(\mathbf{x},t)\boldsymbol{\nabla} u(\mathbf{x},t)] \cdot \hat{\mathbf{n}}_{i,\sigma}\, \mathrm{d}s + \bar{R}_i. \quad \text{(B.6)}$$

To now approximate the integral in (B.6), we take $\bar{u}_i \approx u(\mathbf{x}_i, t)$, $\bar{R}_i \approx \lambda u(\mathbf{x}_i, t)[1 - u(\mathbf{x}_i, t)]$, and use the midpoint rule:

$$\int_{\sigma} [u(\mathbf{x},t)\boldsymbol{\nabla} u(\mathbf{x},t)] \cdot \hat{\mathbf{n}}_{i,\sigma}\, \mathrm{d}s \approx \{[u(\mathbf{x}_\sigma,t)\boldsymbol{\nabla} u(\mathbf{x}_\sigma,t)] \cdot \hat{\mathbf{n}}_{i,\sigma}\} L_\sigma.$$

To approximate $\boldsymbol{\nabla} u(\mathbf{x}_\sigma, t)$, we let $\mathcal{T}_i$ be the set of triangles in $\mathcal{T}(\Omega)$ that have $\mathbf{x}_i$ as a node, and take a triangle $T_k \in \mathcal{T}_i$. Linearly interpolating u over the element T_k,

$$u(\mathbf{x},t) = \alpha_k(t)x + \beta_k(t)y + \gamma_k(t), \quad (x,y) \in T_k, \quad \text{(B.7)}$$

where the coefficients come from the values of u at each vertex of T_k, gives $\boldsymbol{\nabla} u(\mathbf{x},t) = (\alpha_k(t), \beta_k(t))^{\mathsf{T}}$ inside T_k. Thus, our approximation becomes, for each time step,

$$\frac{\mathrm{d}u_i}{\mathrm{d}t} = \frac{D}{V_i} \sum_{\sigma \in \mathcal{E}_i} \left\{ \left[(\alpha_{k(\sigma)}(t)x_\sigma + \beta_{k(\sigma)}(t)y_\sigma + \gamma_{k(\sigma)}(t))\,(\alpha_{k(\sigma)}(t), \beta_{k(\sigma)}(t))^{\mathsf{T}} \right] \cdot \hat{\mathbf{n}}_{i,\sigma} \right\} L_\sigma + \lambda u_i\,(1 - u_i)\,, \quad \text{(B.8)}$$

where $u_i = u(\mathbf{x}_i, t)$ and the $k(\sigma)$ notation is used to refer to the edge σ inside the triangle $T_{k(\sigma)}$.

To complete the approximation, the boundary condition (B.2) is $\mathrm{d}u_i/\mathrm{d}t = \lambda u_i(1 - u_i)$ for points on the boundary. Thus, our discretisation is given by (B.8) in the interior, i.e. the regions bounded by the red curves in Figure 2, while on the red curve we have $\mathrm{d}u_i/\mathrm{d}t = \lambda u_i(1 - u_i)$. The initial condition for this system of ODEs comes from (B.3), letting $u_i = u_0$ on the boundary and $u_i = 0$ in the interior at the initial time. We solve the system of ordinary differential equations using `DifferentialEquations.jl` [54] with the `TRBDF2` algorithm and the `KLUFactorization` linear solver [55, 56] together with the package `FiniteVolumeMethod.jl` [57] that computes the equations.

To assess the accuracy of our implementation of the finite volume, we applied several test cases, including setting up a domain to compare with one-dimensional travelling waves and comparisons with exact solutions. Moreover, we ensured that the size of the mesh used was sufficient by checking that increasing the number of mesh elements did not change the quality of the solution. Tests for the implementation itself are examined clearly in the documentation of the `FiniteVolumeMethod.jl` package [57].

Appendix C. Computing summary statistics from model realisations

In this appendix, we consider the problem of computing the summary statistics $\mu_c(t)$ and $\mu_p(t)$ as defined in the text. We let $C_\tau(t) = \{\mathbf{x} \in \Omega : u(\mathbf{x}, t) = \tau\}$; note that $\tau = 1/2$ in the text. The objective is to compute the area and perimeter of $C_\tau(t)$, together with a polygonal representation of $C_\tau(t)$ assuming $C_\tau(t)$ is simply connected or $C_\tau(t) = \emptyset$. In what follows, we instead compute the area of the region where $u(\mathbf{x}, t) > \tau$, i.e. $A(\Omega \setminus C_\tau(t)) = A(\Omega) - A(C_\tau(t))$, where $A(\Omega)$ is the area of Ω and $A(C_\tau(t))$ the area of $C_\tau(t)$. The area of $C_\tau(t)$ is then obtained by simply computing $A(C_\tau(t)) = A(\Omega) - A(\Omega \setminus C_\tau(t))$.

Let us take our triangular mesh $\mathcal{T}(\Omega)$ of our domain, and consider some triangle $T(\Omega)$ with vertices $\mathbf{x}_i, \mathbf{x}_j, \mathbf{x}_k$ and associated solution values at time t given by $u_i = u(\mathbf{x}_i, t)$, $u_j = u(\mathbf{x}_j, t)$, and $u_k = u(\mathbf{x}_k, t)$. The finite volume method allows us to represent $u(\mathbf{x}, t)$ with a linear interpolant inside T, giving

$$u(\mathbf{x}, t) = \alpha x + \beta y + \gamma, \quad (x, y) \in T,$$

where the coefficients (α, β, γ) depend on t; these coefficients are defined in Appendix B. This linearity then implies that, to find intersections of u with the plane $u = \tau$ inside T, we need only consider intersections with the edges. We denote the edge connecting u_i to u_j by $\overrightarrow{u_i u_j}$, and the edge connecting $\mathbf{x}_i$ to $\mathbf{x}_j$ by $\overrightarrow{\mathbf{x}_i \mathbf{x}_j}$. This edge $\overrightarrow{\mathbf{x}_i \mathbf{x}_j}$ is parametrised by $\mathbf{x}(s) = \mathbf{x}_i + (\mathbf{x}_j - \mathbf{x}_i)s$, $0 \leqslant s \leqslant 1$. With this parametrisation, we see that, if an intersection does exist on $\overrightarrow{u_i u_j}$, it occurs when $s^* = (\tau - u_i)/(u_j - u_i)$, in particular at $\mathbf{x}(s^*) = \mathbf{x}_i + (\mathbf{x}_j - \mathbf{x}_i)(\tau - u_i)/(u_j - u_i)$.

Nodal values			Intersection?			Area contribution
u_i	u_j	u_k	$\overrightarrow{u_i u_j}$	$\overrightarrow{u_j u_k}$	$\overrightarrow{u_k u_i}$	
<	<	<	N	N	N	0
<	<	>	N	Y	Y	$A(u_{ki}, u_{jk}, u_k)$
<	>	<	Y	Y	N	$A(u_{ij}, u_j, u_{jk})$
<	>	>	Y	N	Y	$A(u_i, u_j, u_k) - A(u_{ij}, u_{ki}, u_i)$
>	<	<	Y	N	Y	$A(u_{ki}, u_i, u_{ij})$
>	<	>	Y	Y	N	$A(u_i, u_j, u_k) - A(u_{jk}, u_{ij}, u_j)$
>	>	<	N	Y	Y	$A(u_i, u_j, u_k) - A(u_{jk}, u_k, u_{ki})$
>	>	>	N	N	N	$A(u_i, u_j, u_k)$

Table C.2: Possible configurations of the nodal values relative to the threshold τ. In the first three columns, the symbol refers to u_i's value relative to τ. For example, a < in the u_j column means $u_j < \tau$. In the intersection columns, $\overrightarrow{u_i u_j}$ is the edge from u_i to u_j, and the text refers to whether the plane $u(\mathbf{x}, t) = \alpha x + \beta y + \gamma$ can intersect with the plane defined by the plane $u = \tau$, with "N" meaning no intersection and "Y" meaning there is an intersection. The notation $A(u_i, u_j, u_k)$ means the area formed by these points projected onto the plane, and a point u_{ij} denotes the intersection point on the edge connecting u_i and u_j.

By considering the eight possible values of the u_i, u_j, u_k relative to $u = \tau$, we can easily determine whether an intersection exists. These possibilities are shown in Table C.2, which show that we can check each possibility and compute the area accordingly. All the cases in Table C.2, except for the first and last cases, imply that there is a line going through T where $u = \tau$, and the length of this line can be easily computed by simply taking the magnitude of the difference of the intersections on the two associated edges. Moreover, if we are interested in getting a representation

of the leading edge itself for plotting, we can simply store all these intersection points which we can then sort counter-clockwise and clear duplicated intersections, giving a vector of points that can be plotted. For the wave geometry considered in the text, sorting the leading edge is not as simple and so we instead plot the concave hull of these points, computed with the `ConcaveHull.jl` package [58, 59].

Now that we understand how to compute the area of the part of a triangle that is above the plane $u = \tau$, which we denote by A_T, the total area where $u(\mathbf{x}, t) \geqslant \tau$ is given by $\sum_{T \in \mathcal{T}(\Omega)} A_T$, meaning $A(C_\tau(t)) = A(\Omega) - \sum_{T \in \mathcal{T}(\Omega)} A_T$. Thus, normalising by $A(\Omega)$, we have

$$\mu_c(t) = 1 - \frac{1}{A(\Omega)} \sum_{T \in \mathcal{T}(\Omega)} A_T. \tag{C.1}$$

Similarly, letting ℓ_T be the length of the line in T where $u = \tau$, which is zero if there is no such line, the perimeter of $C_\tau(t)$ is $\ell(C_\tau(t)) = \sum_{T \in \mathcal{T}(\Omega)} \ell_T$, giving $\mu_p(t) = [1/\ell(\partial\Omega)] \sum_{T \in \mathcal{T}(\Omega)} \ell_T$. We note that it is possible to have $\sum_{T \in \mathcal{T}(\Omega)} \ell_T = 0$, which means that there is no part of $u(\mathbf{x}, t)$ where $u > \tau$, but this means the whole of Ω is the void, i.e. $u < \tau$ in all of Ω. Thus, the correct definition is

$$\mu_p(t) = \begin{cases} \dfrac{1}{\ell(\partial\Omega)} \displaystyle\sum_{T \in \mathcal{T}(\Omega)} \ell_T & \displaystyle\sum_{T \in \mathcal{T}(\Omega)} \ell_T \neq 0, \\ 1 & \displaystyle\sum_{T \in \mathcal{T}(\Omega)} \ell_T = 1. \end{cases} \tag{C.2}$$

As described in the manuscript, these quantities μ_S are used to model the distribution that our data $y_S^{i,j}$ are realisations of, namely $Y_S^i \sim \mathcal{N}(\mu_S(t_i; \boldsymbol{\theta}), \sigma_S^2)$. Here we give the formula used for σ_S^2. We simply aggregate all the data for the quantity S into a single set, giving the sample standard deviation

$$\sigma_S^2 = \frac{1}{n_1 + n_2 - 1} \sum_{i=1}^{2} \sum_j \left(y_S^{i,j} - \bar{y}_S^{i,j} \right)^2$$

, where n_i is the total number of data points at $t = t_i$ for $i = 1, 2$, and

$$\bar{y}_S^{i,j} = \frac{1}{n_1 + n_2 - 1} \sum_{i=1}^{2} \sum_j y_S^{i,j}$$

is the aggregated mean of the $y_S^{i,j}$; the second sum in each term denotes a sum over all pore indices j. For the square geometry, $n_1 + n_2 = 41$, and for the wave geometry we have $n_1 + n_2 = 3$.

Appendix D. Reparametrisation of the likelihood function

Here we discuss issues with working with D and λ separately in the likelihood function. For this discussion, we will take $u_0 = 0.2$, but note that the results are the same for any other u_0. To start, let us take our log-likelihood function $\ell(\boldsymbol{\theta} \mid \mathbf{y})$ with $\boldsymbol{\theta} = (D, \lambda)$. We evaluate this log-likelihood over a grid of points, obtaining the surface shown in Figure D.15(a). We see that the log-likelihood in this case is banana-shaped, indicating that D and λ are related [40], and so we would expect problems when trying to compute univariate confidence intervals from the profile log-likelihoods. One way to overcome this issue is to reparametrise in terms of $(D\lambda, \lambda)$, motivated by noting that our likelihood function uses data based on the void boundary which is known to have a speed that depends directly on the product $D\lambda$ [37]. The surface we obtain under this reparametrisation is given in Figure D.15(b), where we see that we can now assign a finite interval to $D\lambda$, meaning we will be able to obtain confidence intervals from the profile likelihood for $D\lambda$, but we can still not assign any upper bound to λ — λ is not identifiable. This latter issue with λ is not important for us, though, as we only need $D\lambda$ to describe the cellular mechanisms driving tissue growth in our experiments.

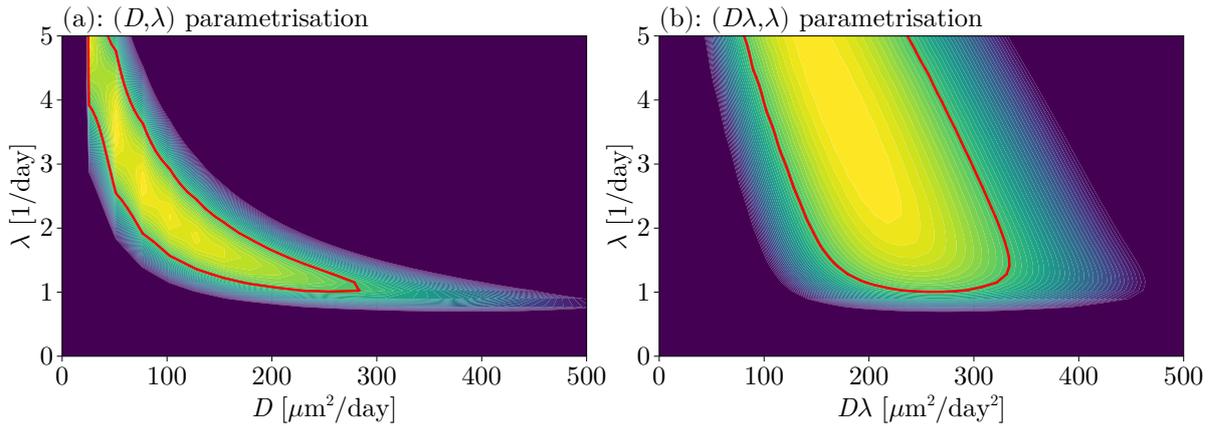Figure D.15: Log-likelihood surfaces for $\ell(\boldsymbol{\theta} \mid \mathbf{y})$ using (a) the (D, λ) parametrisation and (b) the $(D\lambda, \lambda)$ parametrisation. The red curves show the 95% credible region for $\boldsymbol{\theta}$.

We note that, at first glance, it might appear that the surface in Figure D.15(b) could eventually stop on the vertical axis for larger values of λ. We have computed this surface up to $\lambda = 25\,\mathrm{day}^{-1}$ previously and find that this is not the case. Moreover, we note that even the maximum value $\lambda = 5\,\mathrm{day}^{-1}$ shown in Figure D.15(b) is large, as the proliferation time for these cells is typically between half a day to two days, corresponding to a value of λ between $0.5\,\mathrm{day}^{-1}$ and $2\,\mathrm{day}^{-1}$ [16]. Thus, even this value of $\lambda = 5\,\mathrm{day}^{-1}$ is a conservative upper bound, and certainly λ is not identifiable.

Appendix E. Profile likelihood analysis

In this section, we will outline (1) how we compute the MLE, (2) how profile likelihoods are computed, and (3) how prediction intervals are computed.

Appendix E.1. Computing the MLE

The MLE is obtained by maximising $\ell(\boldsymbol{\theta} \mid \mathbf{y})$ over a certain rectangle defined by the bounds on $D\lambda$ and λ. We maximise $\ell(\boldsymbol{\theta} \mid \mathbf{y})$ using NLopt.jl with the derivative-free algorithm LN_BOBYQA [60–62]. To construct an initial estimate for the optimiser, we evaluate the log-likelihood on a 40×40 grid, taking 40 values for $D\lambda$ in $0 < D\lambda < 500$ and 40 values for λ in $0 < \lambda < 5$. We then take the pair $(D\lambda, \lambda)$ in this grid that gives the greatest value for $\ell(\boldsymbol{\theta} \mid \mathbf{y})$, and this then gives the initial estimate we use for the optimiser.

Appendix E.2. Computing profile likelihoods

We describe here how we compute $\ell_p(D\lambda)$ as defined in Equation (8). We use a simple iterative approach, although other approaches that exploit the PDE for improving the computation could be used [63]. The basic idea is to step to the left and right of the MLE $\widehat{D\lambda}$ until we find where $\ell_p(D\lambda) \leqslant c^*$ in each direction, or until we reach the bounds of $D\lambda$; recall that $c^* = -\chi^2_{1,1-\alpha}/2 \approx -1.92$ in this work, taking $\alpha = 0.05$. At each step, we solve the optimisation problem (8) to get a new value for $\ell_p(D\lambda)$ at the given $D\lambda$. This optimisation problem starts with an initial estimate given by the MLE if we have only taken one step, or via linear interpolation of the optimised values for $\lambda^*(D\lambda)$ from the previous two steps, with $\lambda^*(D\lambda)$ denoting the optimised value of λ that together gives the value for $\ell_p(D\lambda) = \max_{\lambda \in \Lambda}[\ell(D\lambda, \lambda)] - \ell^*$, meaning $\ell_p(D\lambda) = \ell(D\lambda, \lambda^*(D\lambda)) - \ell^*$. If we find points on each side of the MLE where $\ell_p(D\lambda) \leqslant c^*$, we stop iterating and fit a spline to the data $(D\lambda_i, \ell_p(D\lambda_i))$, using a bisection algorithm on each side of the MLE to find the two points where $\ell_p(D\lambda) = c^*$. These two points define the endpoints of the confidence interval. This procedure is implemented in the JULIA package ProfileLikelihood.jl [46].

Appendix E.3. Computing prediction intervals

Let us now describe how prediction intervals are computed, following the approach developed by [40]. We note that while we describe the procedure below for propagating uncertainty from the full log-likelihood $\ell(\boldsymbol{\theta} \mid \mathbf{y})$, we could just as easily propagate uncertainty from the profile likelihoods, again following [40]. The results turn out to be essentially the same, and so we only describe the former approach here.

We start with the same 40×40 grid that we use for finding an estimate estimate for computing the maximum likelihood, as described in Appendix E.1. We then find all pairs $\boldsymbol{\theta} = (D\lambda, \lambda)$ in this grid such that $\ell(\boldsymbol{\theta}) - \ell^* \geqslant -\chi^2_{2,1-\alpha}/2$, where $\chi^2_{2,q}$ is the qth quantile of the χ^2 distribution with two degrees of freedom and $\ell^* = \ell(\hat{\boldsymbol{\theta}})$ is the maximum log-likelihood. With $\alpha = 0.05$, $-\chi^2_{2,0.95}/2 \approx -3$. We enumerate the points satisfying this condition as $\{\boldsymbol{\theta}_1, \ldots, \boldsymbol{\theta}_r\}$. For each point $\boldsymbol{\theta}_i$ we compute $\mathbf{q}_i = \mathbf{q}(\boldsymbol{\theta}_i)$ for a prediction function $\mathbf{q}$, giving a sample $(\mathbf{q}_1, \ldots, \mathbf{q}_r)$. Now, letting q_{ij} denote the jth element of $\mathbf{q}_i$, define $\mathbf{q}_L = (\min_{i=1}^r q_{i1}, \ldots, \min_{i=1}^r q_{i|q|})$ and $\mathbf{q}_U = (\max_{i=1}^r q_{i1}, \ldots, \max_{i=1}^r q_{i|q|})$, where $|q|$ is the

length of outputs of $\mathbf{q}$. A parameter-wise prediction interval for $\mathbf{q}$ is then given by $\mathbf{q}_L \leqslant \mathbf{q} \leqslant \mathbf{q}_U$, where the vector inequality $\mathbf{a} \leqslant \mathbf{b} \leqslant \mathbf{c}$ means $a_i \leqslant b_i \leqslant c_i$ for each i.

For our application, the prediction function $\mathbf{q}$ is defined by

$$\mathbf{q}(\boldsymbol{\theta}) = \begin{bmatrix} \mathbf{A}(\boldsymbol{\theta}; \mathbf{t}^*) \\ \mathbf{P}(\boldsymbol{\theta}; \mathbf{t}^*) \\ t_b(\boldsymbol{\theta}) \end{bmatrix}. \tag{E.1}$$

For these functions, we let $\mathbf{t}^*$ be a vector of $m = 361$ equally spaced points between $t = 5$ day and $t = 70$ day. Then, $\mathbf{A}(\boldsymbol{\theta}; \mathbf{t}^*)$ is the vector of coverages $(\mu_c(t_1^*), \dots, \mu_c(t_m^*))$ for the given $\boldsymbol{\theta}$; $\mathbf{P}(\boldsymbol{\theta}; \mathbf{t}^*)$ is the corresponding vector of normalised perimeters $(\mu_p(t_1^*), \dots, \mu_p(t_m^*))$ for the given $\boldsymbol{\theta}$; $t_b(\boldsymbol{\theta})$ is the time at which the area of the void first becomes zero, in particular this is the bridging time for the given $\boldsymbol{\theta}$, computing using the continuous callback interface from `DifferentialEquations.jl` [54] to find when $\mu_c(t) \approx 0$ by applying rootfinding to the function $g(t) = \mu_c(t) - 10^{-9}$.

Appendix F. Likelihood results using area only

In this appendix, we show some of the results when we include only area in the likelihood function rather than both area and perimeter. For the tissue growth predictions, we only show the results at $u_0 = 0.2$, noting that the results for other u_0 are mostly indistinguishable.

Appendix F.1. Square pore

Analogous figures to those in Figures 5–7 are shown in Figures F.16–F.18. The results are very similar, with the main difference being that the uncertainty is much wider than when we also include perimeter information, as should be expected. The differences in the model predictions are also not too distinguishable compared to their counterparts when including perimeter information. Overall, we see that for this data on the square, perimeter does not contribute significantly to our understanding of these effects.
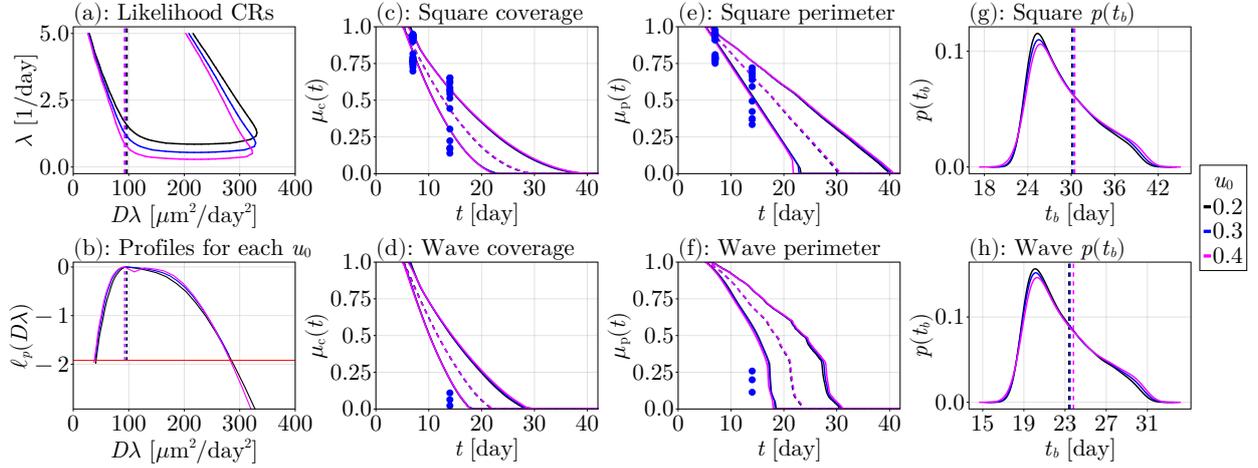

Figure F.16: Likelihood analysis results for the square pore without perimeter information. In (a), the lines give the boundaries of the 95% credible region for θ for each u_0, and the vertical dashed lines show the MLE for $D\lambda$ (see Table 1). The profile log-likelihoods for $D\lambda$ for each u_0 are shown in (b), with the threshold $c^* \approx -1.92$ shown with a horizontal red line and the vertical dashed lines show the MLEs for $D\lambda$. In (c)–(f), predictions for $\mu_c(t)$ and $\mu_p(t)$ on each pore geometry are shown, with the blue dots showing the experimental data, the surrounding solid lines giving 95% prediction intervals for each u_0, and the dashed lines showing the corresponding estimates at the MLE $\hat{\theta}$. The estimates for the PDF $p(t_b)$ of the bridging time on each pore geometry are shown in (g)–(h). The results in (d), (f), and (h) are predictions on the wave geometry using parameters inferred from the square pore data.
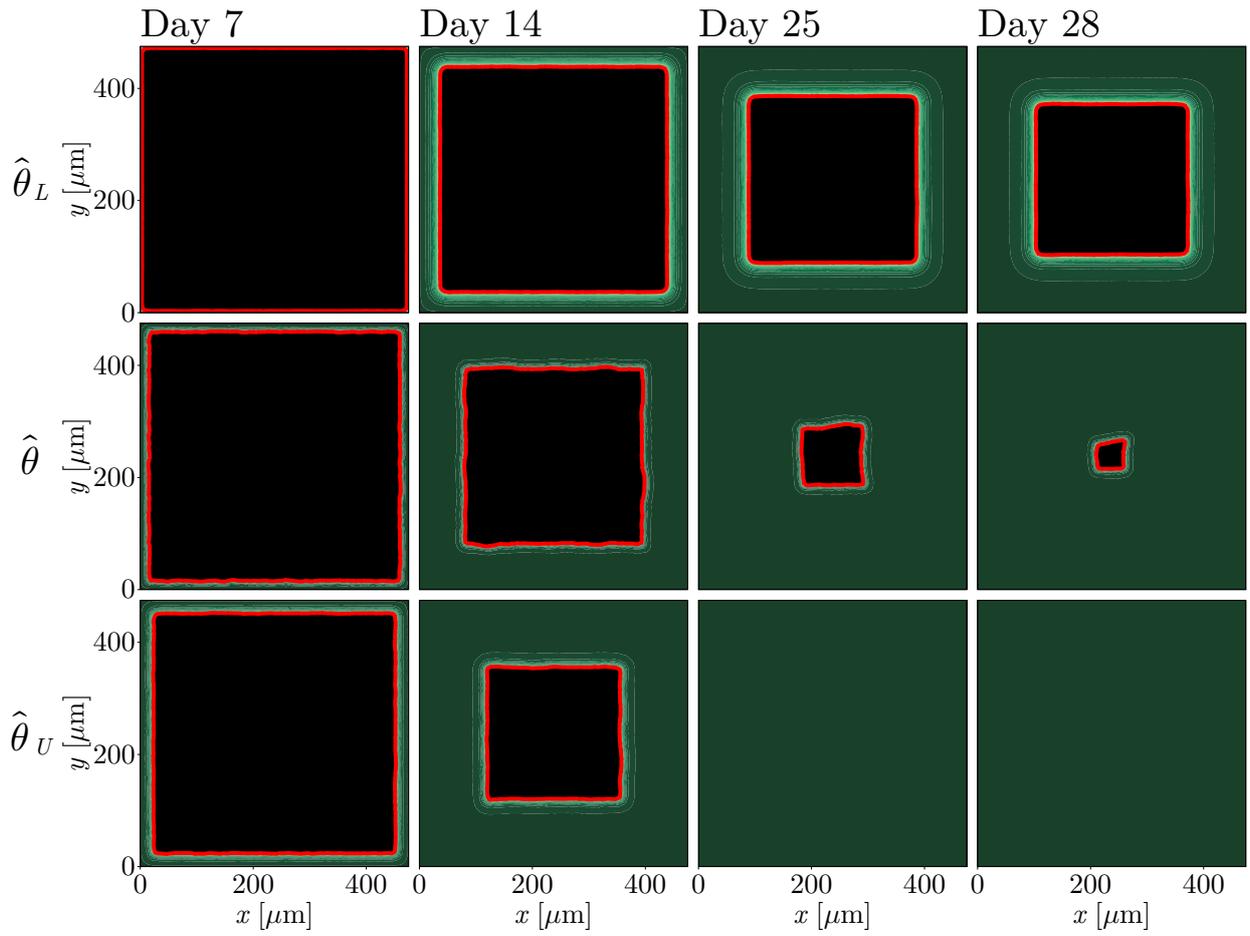
Figure F.17: Model predictions for the variability in the tissue growth behaviour for the square geometry for $u_0 = 0.2$ at days 7, 14, 25, and 28 without perimeter information. The parameters used are $\hat{\boldsymbol{\theta}}_L = (\hat{D}_L, \hat{\lambda}_L) = (41\,\mu\text{m}^2/\text{day}, 1\,\text{day}^{-1})$, $\hat{\boldsymbol{\theta}} = (\hat{D}, \hat{\lambda}) = (19\,\mu\text{m}^2/\text{day}, 5\,\text{day}^{-1})$, and $\hat{\boldsymbol{\theta}}_L = (\hat{D}_U, \hat{\lambda}_U) = (57\,\mu\text{m}^2/\text{day}, 5\,\text{day}^{-1})$.
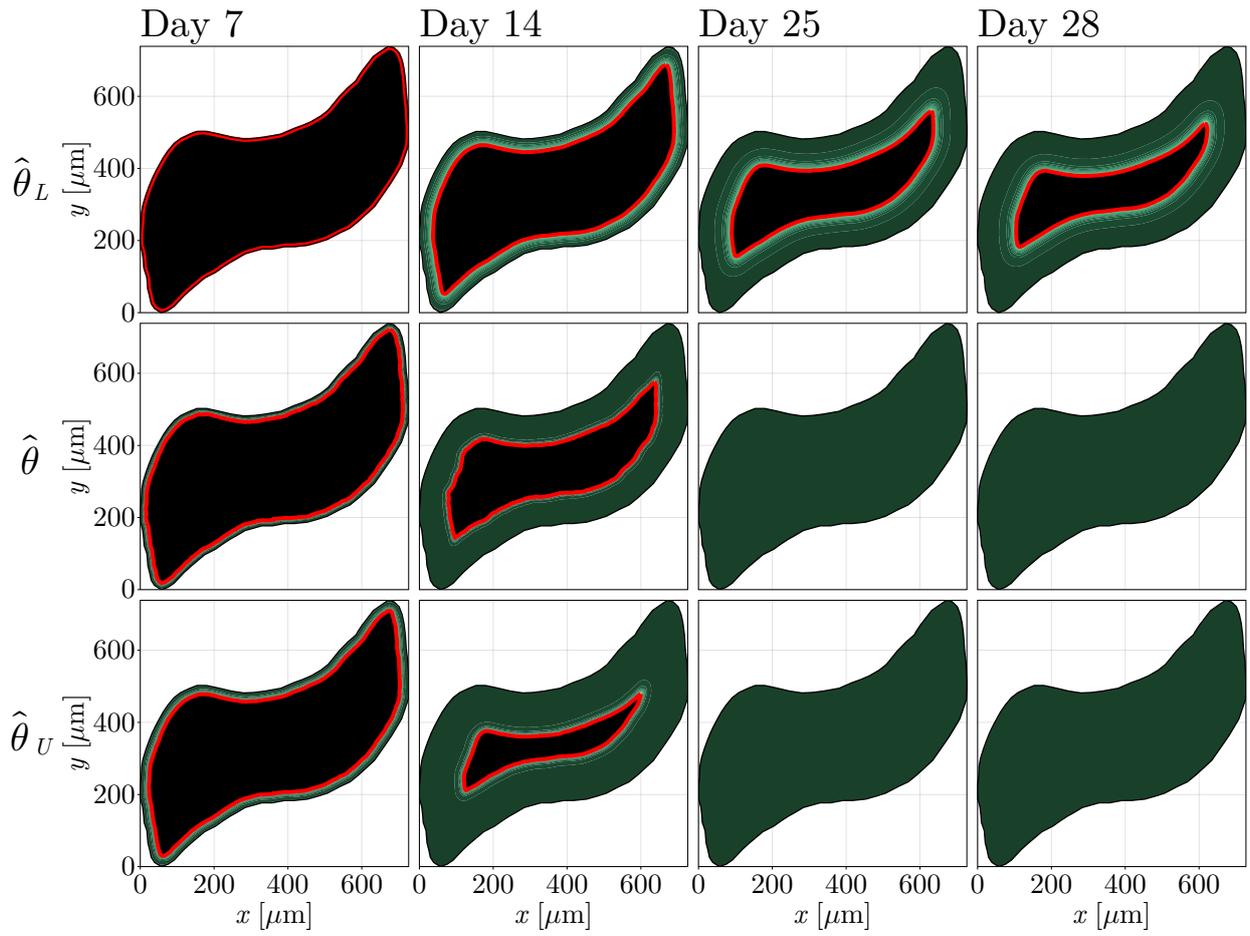
Figure F.18: Model predictions for the variability in the tissue growth behaviour for the wave geometry using results from the square geometry for $u_0 = 0.2$ at days 7, 14, 25, and 28 without perimeter information. The parameters used are $\hat{\boldsymbol{\theta}}_L = (\hat{D}_L, \hat{\lambda}_L) = (41\,\mu\text{m}^2/\text{day}, 1\,\text{day}^{-1})$, $\hat{\boldsymbol{\theta}} = (\hat{D}, \hat{\lambda}) = (19\,\mu\text{m}^2/\text{day}, 5\,\text{day}^{-1})$, and $\hat{\boldsymbol{\theta}}_L = (\hat{D}_U, \hat{\lambda}_U) = (57\,\mu\text{m}^2/\text{day}, 5\,\text{day}^{-1})$.

Analogous figures to those in Figures 8–10 are shown in Figures F.19–F.21. The results are much more problematic in this case than we include area, with the uncertainty significantly wider than before, and $D\lambda$ is no longer identifiable. We do capture the data in our uncertainty intervals, although this is difficult to judge as the uncertainty being so large implies that we might have captured this data regardless. It is impressive, though, that we recover all of the experimental data points on the square. The bridging time distributions in this case cover a much wider range, again due to the large uncertainty in the parameters.
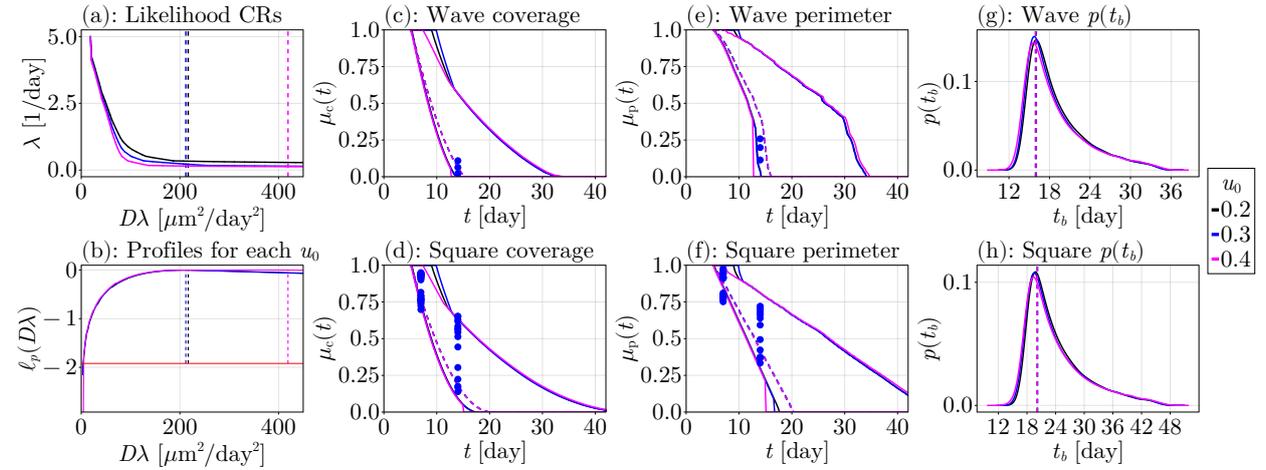

Figure F.19: Likelihood analysis results for the wave pore without perimeter information. In (a), the lines give the boundaries of the 95% credible region for θ for each u_0, and the vertical dashed lines show the MLE for $D\lambda$ (see Table 1). The profile log-likelihoods for $D\lambda$ for each u_0 are shown in (b), with the threshold $c^* \approx -1.92$ shown with a horizontal red line and the vertical dashed lines show the MLEs for $D\lambda$. In (c)–(f), predictions for $\mu_c(t)$ and $\mu_p(t)$ on each pore geometry are shown, with the blue dots showing the experimental data, the surrounding solid lines giving 95% prediction intervals for each u_0, and the dashed lines showing the corresponding estimates at the MLE $\hat{\theta}$. The estimates for the PDF $p(t_b)$ of the bridging time on each pore geometry are shown in (g)–(h). The results in (d), (f), and (h) are predictions on the square geometry using parameters inferred from the wave pore data.
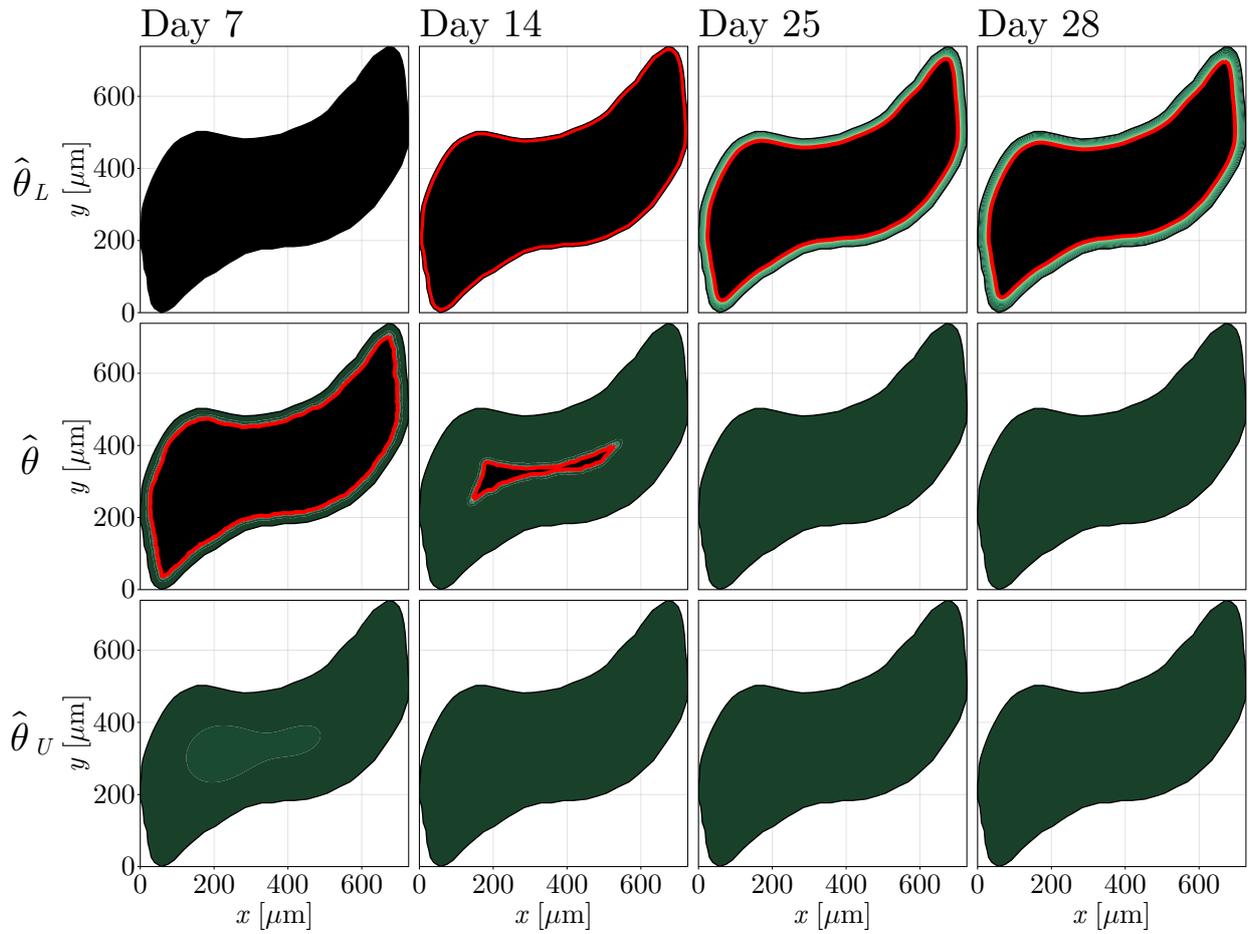
Figure F.20: Model predictions for the variability in the tissue growth behaviour for the wave geometry for $u_0 = 0.2$ at days 7, 14, 25, and 28 without perimeter information. The parameters used are $\hat{\theta}_L = (\hat{D}_L, \hat{\lambda}_L) = (25\,\mu\mathrm{m}^2/\mathrm{day}, 0.2\,\mathrm{day}^{-1})$, $\hat{\theta} = (\hat{D}, \hat{\lambda}) = (22\,\mu\mathrm{m}^2/\mathrm{day}, 10\,\mathrm{day}^{-1})$, and $\hat{\theta}_L = (\hat{D}_U, \hat{\lambda}_U) = (2000\,\mu\mathrm{m}^2/\mathrm{day}, 10\,\mathrm{day}^{-1})$.
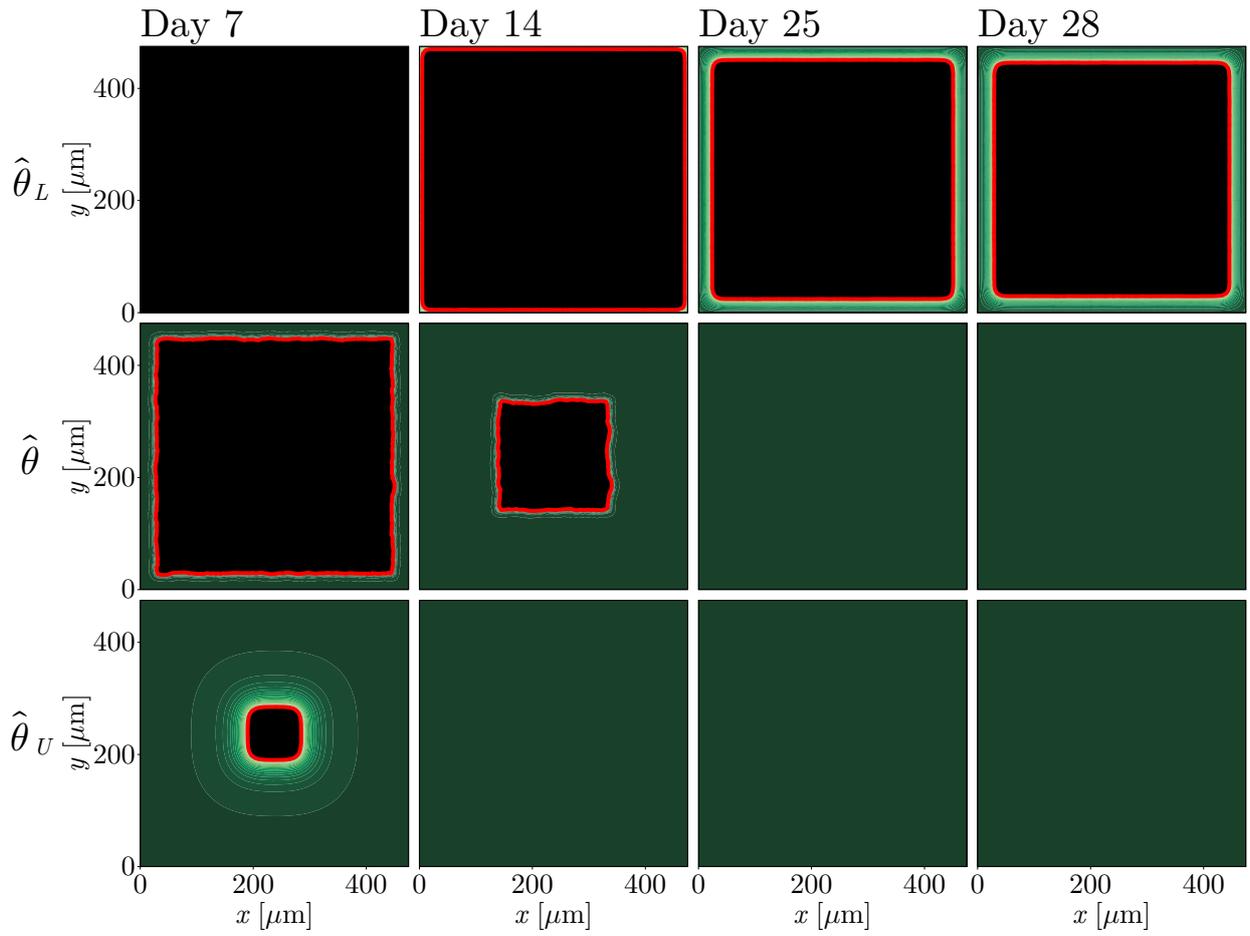
Figure F.21: Model predictions for the variability in the tissue growth behaviour for the square geometry using results from the wave geometry at days 7, 14, 25, and 28 without perimeter information. The parameters used are $\hat{\boldsymbol{\theta}}_L = (\hat{D}_L, \hat{\lambda}_L) = (25\,\mu\mathrm{m}^2/\mathrm{day}, 0.2\,\mathrm{day}^{-1})$, $\hat{\boldsymbol{\theta}} = (\hat{D}, \hat{\lambda}) = (22\,\mu\mathrm{m}^2/\mathrm{day}, 10\,\mathrm{day}^{-1})$, and $\hat{\boldsymbol{\theta}}_L = (\hat{D}_U, \hat{\lambda}_U) = (2000\,\mu\mathrm{m}^2/\mathrm{day}, 10\,\mathrm{day}^{-1})$.